



HAL
open science

Numerical investigation of the effects of distributary bathymetry and roughness on tidal hydrodynamics of Wax Lake region under calm conditions

Hassan Shafiei, Antoine Soloy, Imen Turki, Marc Simard, Nicolas Lecoq, Benoît B. Laignel

► To cite this version:

Hassan Shafiei, Antoine Soloy, Imen Turki, Marc Simard, Nicolas Lecoq, et al.. Numerical investigation of the effects of distributary bathymetry and roughness on tidal hydrodynamics of Wax Lake region under calm conditions. *Estuarine, Coastal and Shelf Science*, 2022, 265, 10.1016/j.ecss.2021.107694 . insu-03661811

HAL Id: insu-03661811

<https://insu.hal.science/insu-03661811v1>

Submitted on 8 Jan 2024

HAL is a multi-disciplinary open access archive for the deposit and dissemination of scientific research documents, whether they are published or not. The documents may come from teaching and research institutions in France or abroad, or from public or private research centers.

L'archive ouverte pluridisciplinaire **HAL**, est destinée au dépôt et à la diffusion de documents scientifiques de niveau recherche, publiés ou non, émanant des établissements d'enseignement et de recherche français ou étrangers, des laboratoires publics ou privés.



Distributed under a Creative Commons Attribution - NonCommercial 4.0 International License

1 Numerical investigation of the effects of 2 distributary bathymetry and roughness on 3 tidal hydrodynamics of Wax Lake region 4 under calm conditions

5 Authors

6 Hassan Shafiei^a, Antoine Soloy^{b*}, Imen Turki^b, Marc Simard^c, Nicolas Lecoq^b, Benoit Laignel^b

7 ^a: Laboratory of Geophysical and Industrial Flows (LEGI), University of Grenoble Alpes, G-INP, CNRS,
8 38000 Grenoble, France

9 ^b: Normandie University, UNIROUEN, UNICAEN, CNRS, M2C, Morphodynamique Continentale et
10 Côtière, 76000 Rouen, France

11 ^c: Jet Propulsion Laboratory, California Institute of Technology, Pasadena, California, USA.

12 *: Corresponding author

13 Abstract

14 In this paper, we investigate the effects of the bathymetry of the floodplain distributaries using a 2-
15 dimensional hydrodynamic model of the Wax Lake Outlet (WLO), delta and floodplain (Louisiana,
16 USA), using Delft3D. Modelling the tidal-fluvial interaction of this region is challenging because of its
17 complex network of low-lying floodplain distributaries and vegetation coverage. This investigation
18 addresses this interaction by generating the evolution of the flood-map that is used in the calibration
19 and validation phase of the Surface Water and Ocean Topography (SWOT) mission. Accordingly, the
20 model is set up for one week of calm conditions from October 14th to 20th in 2016. Boundary
21 conditions applied at the edges of the 36x23 km² domain include the offshore water level with tidal
22 oscillations, the upstream volumetric river discharge rate and wind time-series (applied spatially

23 uniformly) is used in the model. The topo-bathymetry of the domain is a product of the Pre-Delta-X
24 mission; however, it has considerable uncertainties to represent the small distributaries, especially in
25 the forested section of the region. This paper tackles this uncertainty by parametrically enhancing
26 and calibrating the primary Digital Terrain Model (DTM). The performance of the model is assessed
27 using the water-level time series measured by the stations spread throughout the floodplain, delta
28 and main river. The results show that the morphology of the distributaries play a major role in the
29 hydrodynamic of Wax Lake region under calm conditions. The hydrodynamic of the WLO and
30 floodplain is considerably affected by the discharge capacity of the distributaries (changed by editing
31 their width and depth) due to change of the balance between roughness and topographic
32 convergence. In WLO, higher discharge capacity leads to higher overall roughness friction force,
33 thereby dampening the amplitude of the water-level signal and vice versa. On the other hand,
34 increasing the bottom roughness of the WLO increases the water level in the floodplain, with more
35 considerable effect in the low tides. The calibrated model well matches the measurements along the
36 Wax Lake Outlet. However, the main discrepancies are in the stations further away from the WLO.
37 The tests conducted in this research suggest that the excessive roughness due to uneven bed along
38 the distributaries and vegetation are, respectively, the potentially-responsible parameters for the
39 remaining discrepancies in low- and high-tide periods.

40 Keywords

41 Hydrodynamic modeling, Floodplains, Wax Lake region, Delf3D-FLOW, SWOT

42 Highlights

- 43 • The highly complex hydrodynamic of the Wax Lake region is modeled using Delft3D.
- 44 • The bathymetry of the floodplain is enhanced using a parametric process.
- 45 • The model's sensitivity to specific morphological parameters is analyzed.
- 46 • Tidal-fluvial interactions between Wax Lake Outlet (WLO) and its distributaries are discussed.

47 1. Introduction

48 Coastal wetlands act as a major reserve of biodiversity (Sievers et al., 2019; Xie et al., 2019), a highly
49 productive carbon sink (Mcleod et al., 2011; Shields et al., 2017), a water quality and nutrient cycle
50 regulator (Megonigal & Neubauer, 2019; Rivera-Monroy et al., 2011), and a protective barrier against
51 storms and tsunamis (Barbier et al., 2013; Kathiresan & Rajendran, 2005). These regions are subject
52 to a series of complex and interacting natural processes responsible for weathering, marine erosion
53 and flooding hazards (Nicholls et al., 2007). The impacts of these processes are usually site-
54 dependent, changing with bathymetric and energy conditions.

55 The non-linear interactions between these forcings increase the complexity of hydro- and
56 morphological dynamics of coastal areas; for example, (Jay et al., 2015) studied the tidal-fluvial water
57 level in a river and concluded that the relationship is non-linear and non-stationary. Furthermore, the
58 non-linear effects of bathymetry (e.g. channel cross-section and bottom profile), roughness and
59 vegetation on hydrodynamic (e.g., turbulence mixing, dissipation, velocity and water level) make
60 modeling of these regions challenging (Gross & Werner, 1994; Marsooli et al., 2016; Osorio-Cano et
61 al., 2019). In the context of climate change and sea-level rise, predicting the flow of water in tidal
62 rivers and their floodplain is critical. Buschman et al. (2010) developed a model to predict the flow
63 division in a tidal junction, showing that the inlet stokes transport is not necessarily equal to the
64 Eulerian return transport and depends on many factors such as channel depth, width, length,
65 roughness and asymmetry. (Sassi et al., 2011) continued the work of (Buschman et al., 2010) and
66 concluded that the neighboring channels affect each other's hydrodynamic. Further, (Hoitink & Jay,
67 2016) reviewed the methods for analyzing water level and inundation extent in various tidal rivers.
68 Moreover, (Leonardi et al., 2015) studied the river-tide interaction in a delta and concluded that
69 regardless of the strength of the fluvial discharge, tide strongly affects the hydrodynamic of the
70 delta.

71 This complexity increases especially in vegetated environments (Zhang et al., 2018). Indeed, the
72 presence of vegetation has a significant impact on coastal wetland hydrodynamics by obstructing the
73 water flow (Temmerman et al., 2007). Furthermore, it changes the bottom erosion resistance,
74 turbulence mixing, flow resistance, wetted area, and inundation (Al-Asadi & Duan, 2017; Baptist et
75 al., 2007; Horstman et al., 2014, 2018; Hu et al., 2015; Jay et al., 2016; Nardin et al., 2016).

76 The Mississippi River Delta region is an ideal study site to understand the multi-scale evolution of
77 coastal wetlands with a long-term and dense in-situ instrument network. In particular, the evolution
78 of the Wax Lake Delta (WLD, western region of the Mississippi River Delta floodplain) can be tracked
79 from its initiation because it was naturally formed after the construction of the Wax Lake Outlet
80 (WLO) by the United States Army Corps of Engineers (USACE) in 1942 (Hanegan, 2011). Extensive
81 research has been conducted in the WLD region to understand its hydrodynamics (Hanegan, 2011; F
82 Xing et al., 2013; Zhang, 2015), morphodynamics (Edmonds & Slingerland, 2007; Parker & Sequeiros,
83 2006; Fei Xing et al., 2017), and biological and ecological evolution (Carle, 2013; Olliver & Edmonds,
84 2017; Shaffer & Sassert, 2018). However, the previous models focused on the WLO and Wax Lake
85 delta at its mouth (Christensen, 2017; Hanegan, 2011; Fei Xing et al., 2017; Zhang, 2015); they
86 generally neglected the dynamics of the intertidal wetlands on either sides of the WLO. One of the
87 main challenges is the lack of detailed Digital Terrain Model (DTM) which is an essential requirement
88 in hydrodynamic modeling of plain regions like Wax Lake floodplain. In these types of environments,
89 small topographic variations influence the water storage and flow velocity considerably more than
90 those in the regions with steep slopes (Jung & Jasinski, 2015).

91 In the framework of the Surface Water and Ocean Topography (SWOT) mission, the results of this
92 study will be used in the validation and calibration phase by providing the map of the water-surface
93 evolution in one of the sites being studied in the SWOT mission (i.e., Wax Lake region); the particular
94 focus is on the hydrodynamics of the WLO floodplain. One of the objectives of the SWOT mission is
95 to provide surface-water topography measurements along rivers, lakes, streams, and wetlands and

96 over the ocean surface using swath altimetry with the orbit repeat period of about 21 days. The
97 spatial resolution of SWOT products would be 1 km and 100 m for the ocean and land water
98 respectively. Furthermore, the elevation accuracy would be about 3 cm for ocean and 10 cm for land
99 water surface (Durand et al., 2010; Neeck et al., 2012; Marc Simard et al., 2019). The results of the
100 current investigation would be utilized as an input into the SWOT simulator (e.g., Gaultier et al.,
101 2010; Gomez-Navarro et al., 2018). Therefore, the spatial and temporal resolutions of the current
102 modeling are chosen accordingly.

103 Within the context of SWOT, this paper presents the use of a hydrodynamic models for SWOT
104 calibration and validation in a flat intertidal area containing river, delta and a complex network of
105 floodplain distributaries. An approach is also introduced to calibrate the bathymetry of the vegetated
106 floodplain which initially may not have accurate digital elevation models. Knowledge of water-
107 surface elevation summarizes information about the different acting physical forcing, as well as their
108 interaction with one another and with the local geomorphology. With this in mind, this study's goal is
109 to address the following questions:

- 110 • Which and how do some local environmental settings influence the water level variability?
- 111 • What combination of geomorphological parameters such as the drag coefficient and channel
112 geometry allow the best reconstruction of the Wax Lake region's hydrodynamics for calm
113 conditions?
- 114 • How is the tidal oscillatory signal transformed along its propagation through the distributary
115 channel network?

116 In Section 2, we introduce the study site. In Section 3, the Delft3D model and its configuration are
117 summarized, with a description of the processing methodologies applied to the hydrodynamical and
118 morphological data. The model results are discussed in Section 4 with a particular attention given to
119 having the best result following a systematic procedure rather than a manual one (so that it can be
120 applied to other areas and scales). The respective results of the bathymetry calibration will also be

121 discussed in this section. Furthermore, some suggestions are explained to further improve the
122 model. Conclusive remarks will be presented in the fifth and final Section.

123 2. Study Site

124 The WLO is an artificial canal connecting the Wax Lake and the Gulf of Mexico that was built by the
125 USACE in 1942 in order to divert 30% of the flow from the Atchafalaya River to the sea and prevent
126 flooding in the surrounding cities (Davidson et al., 1988). The construction of the canal delivered 34
127 Megatons of sediment per year (Kim et al., 2009), naturally forming the Wax Lake Delta that pro-
128 graded 8 km toward the sea in 64 years. The evolution of this delta is not controlled, providing an
129 ideal large scale experiment to study river delta formation (Christensen, 2017; Hanegan, 2011; Fei
130 Xing et al., 2017; Zhang, 2015). Along with the Atchafalaya River Delta, the Wax Lake Delta is one of
131 the only places in the Mississippi River Delta region subject to prograding, while the rest of the coast
132 is receding (Hiatt, 2013). The measured discharge at the Calumet station located 18 km north of Wax
133 Lake delta (shown with grey circle in Figure 1a) has an average flow of 2500 m³/s with annual floods
134 exceeding 5000 m³/s (Hiatt, 2013; Rouse Jr et al., 1978). Furthermore, the station (shown with white
135 circle in Figure 1(a)) at the southeastern corner of the domain is where the tidal inlet conditions were
136 measured; the yellow and orange circles represent the observation point used for evaluations of the
137 results. Wax Lake outlet's depth is about 25 m upstream, 20 m downstream and 5 m in the delta fan
138 (Figure 1 b and c).

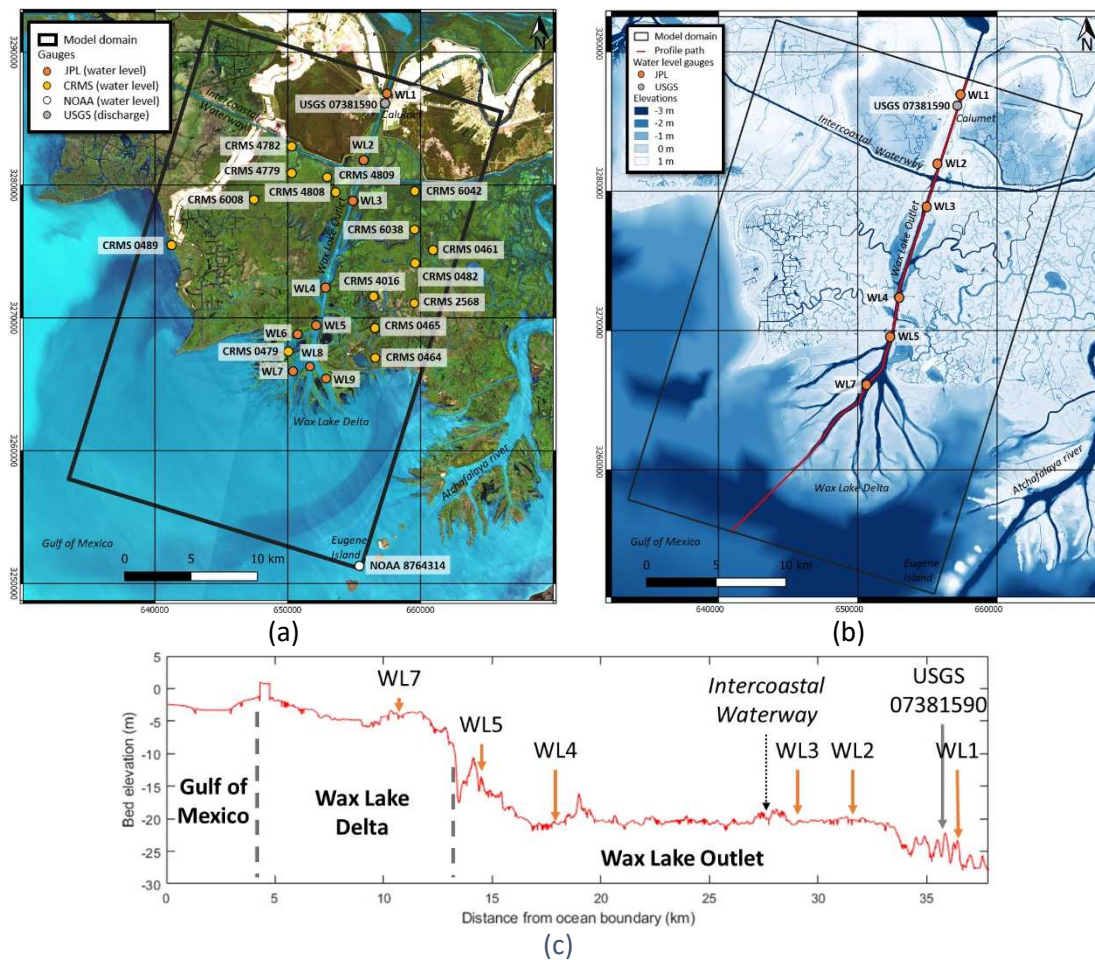


Figure 1– (a) The study area and the location of the measurement stations used for model input and validation of the results, (b) The calibrated DTM of the study area and (c) the bottom profile of the WLO and the main pass of the Wax Lake Delta. (NAVD88)

139 3. Methodological approach

140 The present study was realized using the Delft3D two-dimensional (depth-averaged) model fed with
 141 data provided by NASA/Jet Propulsion Laboratory (JPL), the United States Geological Survey (USGS),
 142 the National Oceanic and Atmospheric Administration (NOAA) and Google¹. In this section, these
 143 data and tools will be described.

144 3.1. Delft3D

145 The Delft3D is a package of integrated modules developed by Deltares to simulate flow
 146 hydrodynamics, sediment transport, morphological processes, and water quality aspects in the

¹ <https://mt1.google.com/vt/lyrs=r&x={x}&y={y}&z={z}>

147 coastal, river, and estuarine areas (Roelvink & Van Banning, 1995). The hydrodynamic module is
148 named as Delft3D-FLOW and solves the two-dimensional (depth-averaged) and three-dimensional
149 unsteady shallow-water equations (Lesser et al., 2004). The two-dimensional depth-averaged
150 momentum equations are obtained by integrating the three-dimensional hydrostatic shallow-water
151 equations from the bottom to the free surface (in the 3D model, the third dimension ,i.e. depth, is
152 scaled from -1 to 0 (Gerritsen et al., 2008; Stelling & Van Kester, 1994)).

153 Delft3D-FLOW wetting-drying algorithm is effective and accurate for the flows with large gradients of
154 water level. It obtains the water level in the center of each cell using the computed water depth at
155 the cell nodes. Then, it calculates the total water depth at each velocity point. If the value is lower
156 than the half of the user-defined depth threshold, the water-depth is set to zero at that point. Finally,
157 if all four velocity points in a cell are zero, the cell is considered as dry (i.e., it becomes a closed
158 boundary). The cell will be considered wet again if the total water depth becomes higher than that
159 threshold (Deltares, 2014).

160 3.2. Model description

161 In the present model setup, tide-induced water elevation, river-discharge flow rate, and wind
162 velocity were used in order to simulate the hydrodynamics of Wax Lake Delta and surrounding
163 intertidal area. The desired simulation period ranges from October 14th, 2016 at 00:00:00 UTC to
164 October 20th, 2016 at 00:00:00 UTC. However, to give the simulation enough time so that the inlet
165 tide reaches the northern stations, it was necessary to start the computation earlier in order to
166 ensure the model converges to a steady state in the distributary channels in the wetlands. For this
167 purpose, the simulation was set to start on October 2nd, 2016.

168 3.2.1. DTM data and processing

169 The calibrated Digital Terrain Model (DTM) used in this research is presented in Figure 1b. The
170 original version was produced by the Pre-Delta-X mission (M. W. Denbina et al., 2020). It is a 10-
171 meter-resolution DTM derived from merging of four different data sources, each with different

172 horizontal and vertical accuracies. One of the main data source is Shaw et al. (2016), with root-mean-
173 square error of 0.1 m (by comparing the bathymetric surfaces to surveyed lines). More information
174 about the uncertainty of the sounder measurements they used as well as the effect of the
175 interpolation they performed is explained in section 7.2 of (Whaling & Shaw, 2020). The other three
176 data sources include the land topography from the USGS National Elevation Dataset (NED) (Gesch et
177 al., 2002), with a global-scale RMSE of 2.4 m; a bathymetry of the bay by Xing et al. (2017); and sonar
178 measurements collected during Pre-Delta-X campaigns in May 2015 and November 2016 (M. W.
179 Denbina et al., 2020).

180 However, the primary bathymetry was not sufficiently accurate to allow for a realistic flow of water
181 especially into the forested floodplain. This is in part due to limited bathymetric measurements in
182 areas covered by vegetation. In this investigation, a calibration approach (with the potential
183 applicability to a more extended DTM of the region covering the Atchafalaya river and floodplain) is
184 suggested to modify the original DTM. For achieving this goal, Google-map water mask (Google, n.d.)
185 proved to be detailed enough to be used as a raster selector in modifying the distributary network of
186 the primary DTM. The original pixel size of the water mask is 60x60 cm², which is upscaled to 10x10
187 m² to match the primary DTM to be modified. This Google-Maps water mask (Google, n.d.) is then
188 used to improve the channel network configuration, depth, and width across the floodplain. The
189 modification procedure includes (1) selecting the pixels that need to be modified and (2) digging the
190 selected pixels adequately. Using the QGIS raster calculator¹, the initial DTM is used to identify the
191 floodplain (by choosing $-3.35 < \text{depth} < 2$, in meters) from the Wax Lake Outlet, Wax Lake Delta and
192 Gulf of Mexico. Furthermore, the water-mask raster values (between the values corresponding to
193 water and dry land) are used to control the connectivity of the distributaries in the floodplain (using
194 the QGIS raster calculator). However, increasing the connectivity makes the distributaries wider
195 (since the values of the pixels on the edges of the distributaries and those increasing the connectivity
196 are almost the same). Thus, the connectivity must be increased carefully so that the width of the

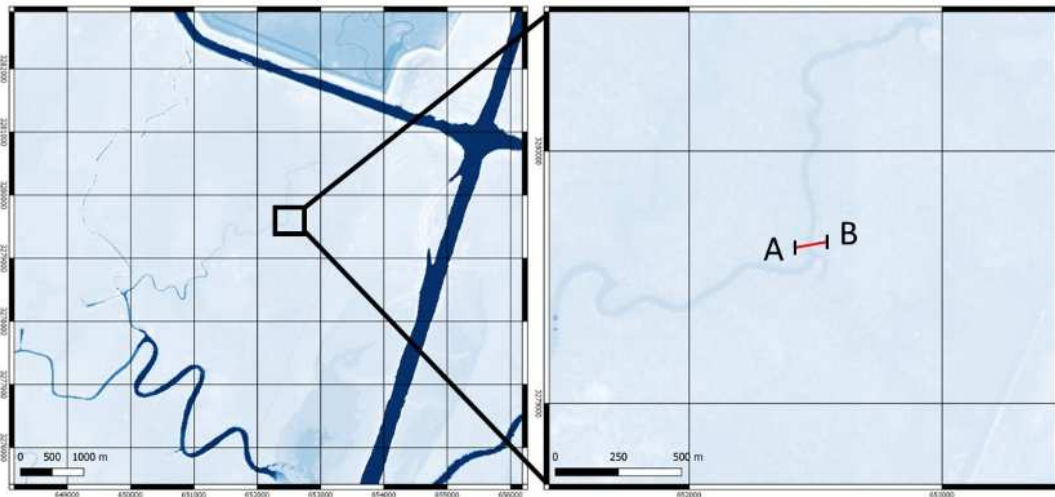
¹ <http://qgis.osgeo.org/>

197 distributaries is not exaggerated. In this study, two connectivity configurations (see Figure 2) are
198 examined. Hereafter, the resultant modified DTM using these two configurations are distinguished
199 by using either 'wide' or 'narrow' in their respective names. In the next step, the depth of the
200 selected pixels is increased uniformly by subtracting a constant value from their terrain elevation
201 using the primary DTM. However, since no data are available regarding the actual depths of these
202 channels, different digging values are tested, and their respective modelled water levels are
203 compared. Here, the results of the cases in which the selected pixels are dug by 1, 1.5, 2 and 2.5
204 meters are presented and discussed (note that the values out of this range result higher water-level
205 deviations from the measurements). Hereafter in this paper, they are distinguished by their
206 respective digging values (i.e., either 1 m, 1.5 m, 2 m or 2.5 m) in their names (note that the grid is
207 kept the same as will be explained in Section 3.4). More details about the effects of these
208 modifications on the hydrodynamics are presented in the section 4.1.

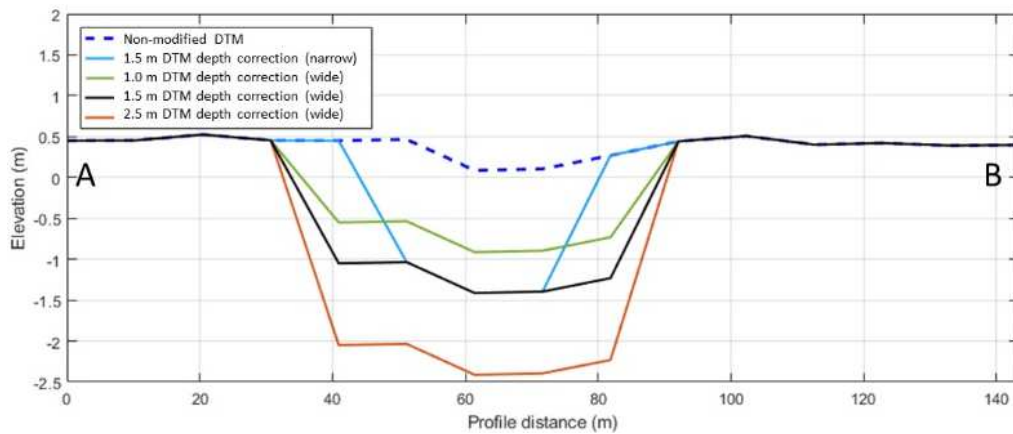
209 Seven versions of the modified DTMs are presented in this study (hereinafter named as narrow 1 m,
210 narrow 1.5 m, narrow 2 m, narrow 2.5 m, wide 1 m, wide 1.5 m and wide 2.5 m). Figure 2 compares
211 some of these DTMs by illustrating the depths and widths of a distributary channels in the
212 northwestern forested part of the Wax Lake wetlands. Part (a) shows a selected section of the
213 primary DTM as well as the distributary channel whose cross-section is illustrated in part (b) of Figure
214 2. And parts (c)-(f) compare the network of the distributary channels in the north-western side of
215 WLO in these modified DTM versions. Figure 2c shows the DTM modified by digging the distributary
216 channels by 1.5 meters (in this paper, it is named as narrow 1.5-meter depth DTM correction). The
217 other parts (d), (e) and (f) present the distributaries created using a wider range of pixels which lead
218 to more channel connectivity and wider channels (they will be named as 'wide' followed by their
219 depth correction value).

220 Note that the resolution of the DTM is higher than that of the model; therefore, *Grid Cell Averaging*
221 (in Delft3D) is used to generate the bathymetry of the model (i.e., *.dep file). Therefore, to test the

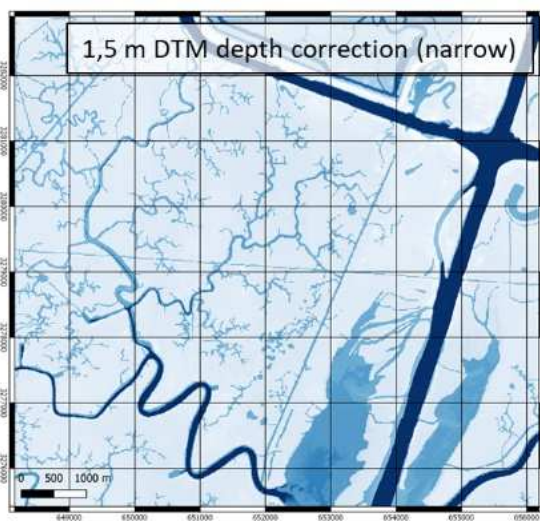
222 effects of the flattened bed of the distributaries, the Delft3D depth file (*.dep), rather than DTM, is
223 edited. The bed of the distributaries is flattened by simply replacing all the computational cells within
224 a certain depth range by a constant value.



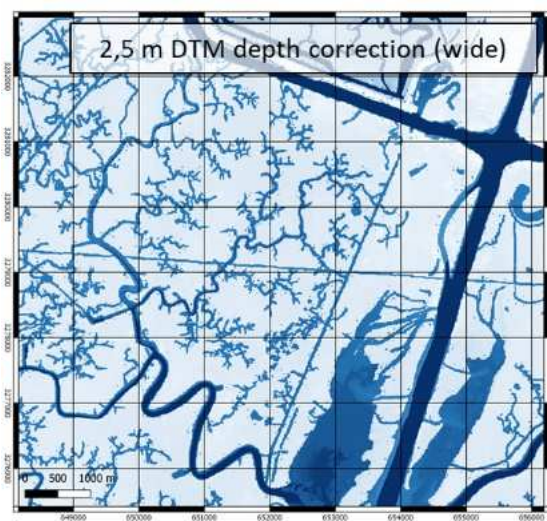
(a)



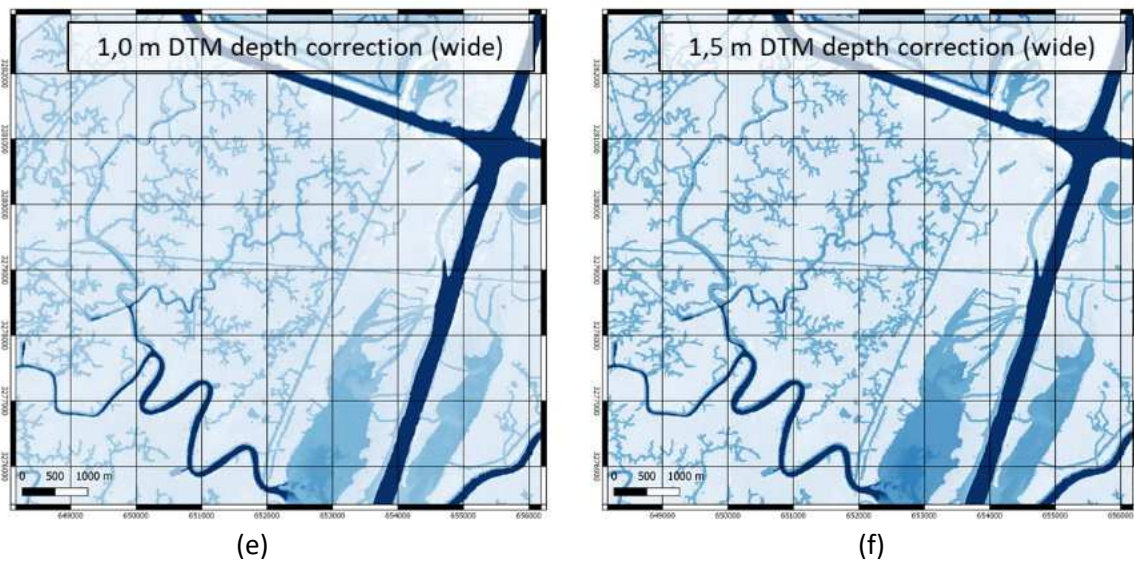
(b)



(c)



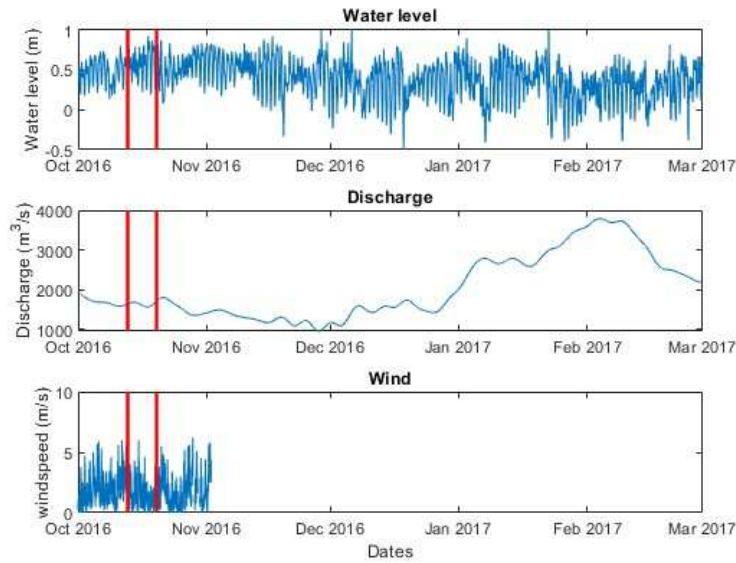
(d)



225 *Figure 2 - Illustration of the northwestern floodplain section of some of the modified DTMs (a) : primary DTM, (b) : bottom*
 226 *cross-sectional changes of an arbitrary distributary channel shown in part (a), (c)-(f) : the top view of the same section as*
 227 *part (a) corresponding to four selected versions of DTM modification.*

228 3.2.2. Input parameters

229 Water level and wind data (Figure 3) were measured at three-minute interval at NOAA's Eugene
 230 Island station 8764314. The vertical reference used for the water levels is the North American
 231 Vertical Datum of 1988 (NAVD88). We can observe that the river discharge is almost constant in
 232 comparison to other periods, and the average water level and wind speed are 0.52 m and 1.82 m/s
 233 respectively. Furthermore, the WLO flow rate was measured every three minutes at USGS' Calumet
 234 station 07381590.



235

236 *Figure 3 - Time series of water level, river discharge, and wind speed used within the model's time range (vertical red line)*

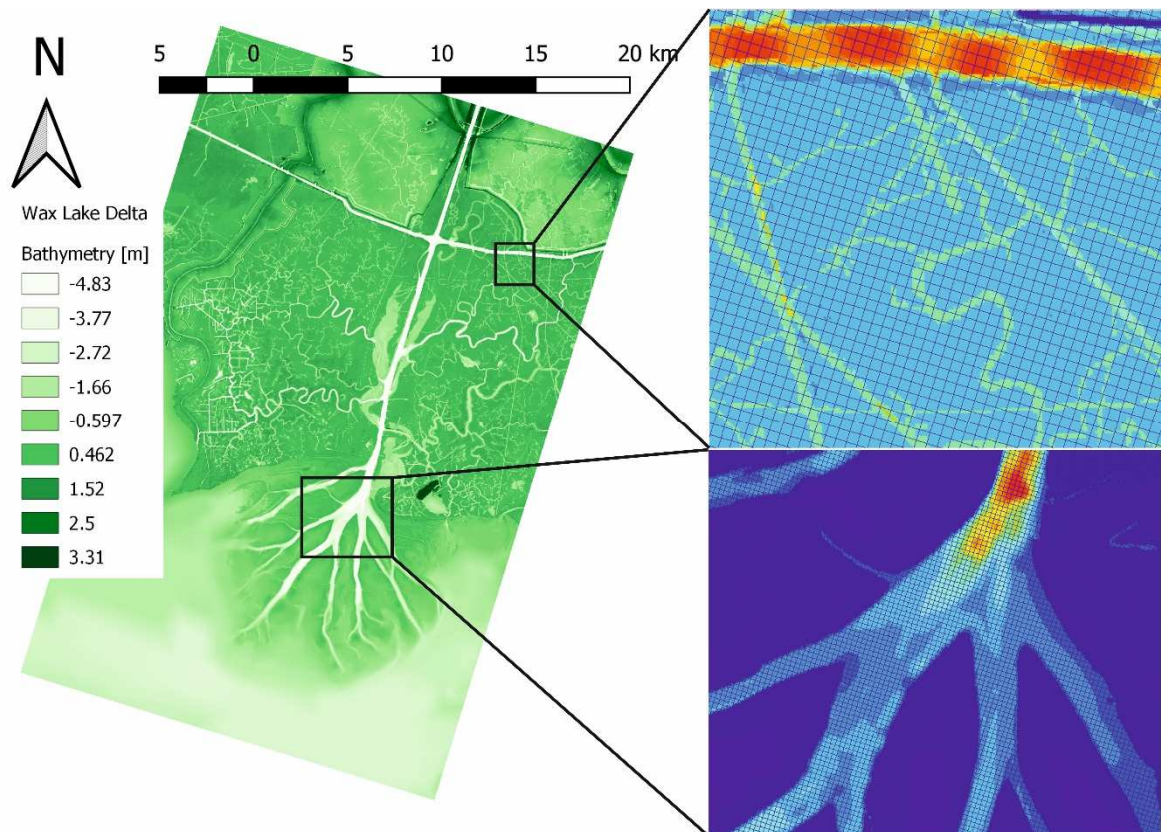
237 **3.3. Evaluation data**

238 In-situ measurements of water level from the USGS Coastwide Reference Monitoring System (CRMS)
 239 stations (Steyer, 2010) and nine additional stations installed specifically for the AirSWOT campaign
 240 (M. Denbina et al., 2019) were used for evaluating the model. The measurements of the CRMS
 241 stations (Figure 1a) are according to vertical reference NAVD88. Moreover, the nine temporary
 242 stations recorded water level using pressure transducers (Solinst levellogger®) between October 13th
 243 and 20th of 2016 (vertical datum NAVD88) to validate AirSWOT measurements (M Simard et al.,
 244 2020), shown in Figure 1a as WL1-WL9. The above-mentioned stations are located throughout the
 245 numerical domain: WL1 to WL5 are along the Wax Lake Outlet, and WL6 to WL9 as well as CRMS0479
 246 are in the Wax Lake delta. Some of stations are near the eastern coast of the domain (i.e., CRMS0464
 247 and CRMS0465) and some are in the eastern marshland (i.e., CRMS2568 and CRMS4016). There is
 248 one station on the coast near the western boundary of the domain (i.e., CRMS0489) and one along
 249 the bank of intercoastal water way (i.e., CRMS4782). The rest of the stations are on the western (i.e.,
 250 CRMS6008, CRMS4779, CRMS4808, and CRMS4809) and eastern (i.e., CRMS 6042, CRMS6038, and
 251 CRMS0461) forested floodplain respectively.

252 3.4. Numerical model configuration

253 The modified DTMs explained in section 3.2.1 (with the resolution of $10 \times 10 \text{ m}^2$) are interpolated
254 into a regular uniform grid with the resolutions of $46 \times 45 \text{ m}^2$ (Figure 4, with a 0.25-minute time-
255 step). Interestingly, using a finer mesh increases the computational cost while the results (especially
256 during low tide) do not improve considerably. This may be related to the high uncertainty of the DTM
257 in representing the bottom profile of the distributaries, as explained by (Jung & Jasinski, 2015). As
258 also will be explained later in Section 4.2, flattening the bed of the distributaries (i.e., replacing the
259 depth values along the distributaries with a constant depth) improved the results during the low tide
260 periods, emphasizing on the need to revise the bottom depth profiles along the distributaries
261 especially in the forested region of the floodplain. However, finding an approach to revise the DTM
262 to represent a more precise bottom profile of the distributaries remains a challenge. As explained in
263 Section 3.2.1, the constant-depth distributaries tested in the current model are obtained by revising
264 the *.dep file in the Delft3D model rather than the DTM file.

265 In this paper, we evaluate the model at the resolution accepted for the SWOT simulator, i.e. 50×50
266 m^2 . Furthermore, especially at the stations experiencing lower water depths, the threshold for
267 drying/wetting procedure (explained in Section 3.1) becomes important. In this model, *Threshold*
268 *depth*=0.01 m was found to be a suitable choice.



269

270 *Figure 4 illustration of the uniform structured grid (the right-hand-side of the figure, with resolution of 46 * 45 m²) used in*
 271 *the simulations presented in this paper*

272 In the first stage, we use uniform Manning's coefficients of $n=0.018, 0.02, 0.022,$ and $0.025 \text{ s/m}^{1/3}$ for
 273 all the modified DTMs, choose most suitable value for Manning's coefficient, then select the best
 274 case (explained briefly in Section 4.1). Afterwards, we use non-uniform Manning's coefficient for the
 275 best case chosen in the previous stage. Two approaches are tested to apply non-uniform Manning's
 276 coefficient: (1) applying different values of Manning's coefficient for each region using *Polygon* (in
 277 Delft3D) in Delft3D-QUICKIN (dividing the domain into five sections of main river, delta, eastern
 278 floodplain, western floodplain and Gulf of Mexico) (2) using the depth of the cells as a criterion to
 279 choose their respective allocated Manning's coefficient. This is done simply by replacing the depth
 280 values (in **.dep* file in Delft3D) within a certain range by the corresponding Manning's coefficient,
 281 then use the file as a roughness input file (**.rgh* file in Delft3D). In this study, the focus is on
 282 approaching an automatic procedure with the least manual settings involved so that it can also be
 283 applied in future studies. Furthermore, each station in the domain behaves differently (i.e., some
 284 need to be drained more in the low tides, some need to receive less water mass, some have longer

285 inundation periods, etc.) which makes predicting the appropriate Manning's coefficient for each
286 region difficult, especially considering that some of the adjacent stations are interconnected through
287 multiple distributaries). It was also observed that due to small depth variation across the flood plain,
288 there were no significant differences between the results of the two approaches (not presented
289 here); the second approach is preferred due to its simplicity and smoother roughness transition to
290 the adjacent cells.

291 Four types of boundary conditions (BCs) are used in the domain. The tides enter the domain
292 perpendicularly to the southern boundary using water-level time-series, and the river discharge is
293 inputted as discharge time-series from the intersection line of the WLO and the northern boundary.
294 The other parts of the northern boundary are enclosed by levees and thus are closed boundaries in
295 the model. The western boundary is completely isolated behind levees, outside of the domain of
296 interest. On the other hand, the eastern boundary is within the floodplain. Comparing the results of
297 stations nearby this boundary, we found that a wall BC produced more realistic results than the
298 Neumann BC. The Neumann BC produced excessive inlet of water mass when the cells along the
299 eastern boundary were dried after each high-tide period (for future studies, we recommend to
300 include the Atchafalaya river and floodplain also). For the sea section of the eastern and western
301 boundaries, considering the fact that the tides are imposed perpendicular to the southern boundary
302 and neglecting the alongshore water-level gradient, the Neumann BC was found suitable (Deltares,
303 2014). It should be noted that the boundary conditions at the inlet and outlet of the intercoastal
304 waterway (ICWW) are considered to be wall BC, meaning that its flow within the domain is
305 neglected. As explained by Hanegan (2011), the reasons behind this assumption are, firstly, the flow
306 in this channel is relatively small in comparison to the one in Wax Lake Outlet. Secondly, the average
307 flow exchange between the two channels is negligible (i.e., the flow rate entering the domain
308 through ICWW is approximately equal to the one exiting through it on the other side of the domain),
309 making its effects on the hydrodynamic of the region small.

310 Furthermore, to test the effects of vegetation and support the assumption of neglecting them in this
311 work, Baptist 2 formulation (Baptist et al., 2007) is used in this Delft3D model (the results are not
312 presented in this paper due to the negligible effect in improving the results). This formulation is
313 classified as the vegetation area class of trachytopes in which a vegetation-induced flow resistance
314 term is added to the momentum equation. This gives the advantage of separating the vegetation
315 effects from the bed roughness. In this model, first, the computational cells to include vegetation are
316 selected using the Sentinel-2 radar data (Thomas et al., 2019) representing three vegetation
317 coverage types of forest, marsh and bare. Then, for each cell, rough values for the density of forest
318 and marsh are calculated using the same Sentinel-2 radar data. Finally, some sensitivity tests are
319 performed to examine the effects of vegetation input parameters (e.g., vegetation height, density
320 and drag coefficient); however, none of the tests improved the results.

321 4. Results and discussions

322 4.1. Bathymetry Calibration

323 The most suitable DTM is chosen following a calibration approach by comparing their respective
324 modeled water level with the observations (Figure 5). The model outputs are compared to the
325 observed dynamics in the Wax Lake Outlet's main channel and delta using the data recorded during
326 the JPL field campaign of November 2016 (M Simard et al., 2020) and in the intertidal floodplain
327 using the CRMS data (Steyer, 2010). While the original DTM, left some of the CRMS stations located
328 in the floodplain dry (e.g., CRMS6042), even after 18 days of simulation (i.e., 02/10/2016 -
329 20/10/2016), it was found that modifying the DTM solved the problem of the dry stations. This
330 calibration approach gives a good insight on how the bathymetry of the distributary channels
331 changes the water-level variability of the whole region in calm conditions, as explained hereinafter.
332 This approach is suggested to be used for simulating the dynamics of an extended domain of the
333 region in the future works.

334 As explained in Section 3.4, The DTM is calibrated using different uniform Manning's coefficients. The
335 effect of Manning's coefficient on all the modified DTMs follows the same trend: generally, high-tide
336 water levels do not change considerably while low tide ones decrease with lower values of Manning's
337 coefficient. This effect is favorable for some stations, but not for the others. For instance, lower
338 (higher) roughness values lead to underestimation (overestimation) of low-tide water level along the
339 WLO (in the floodplain). Consequently, among the values of $n=0.018$, 0.02 , 0.022 , and $0.025 \text{ s/m}^{1/3}$,
340 $n=0.02 \text{ s/m}^{1/3}$ is chosen as the best compromise to be used for studying the effects of the width and
341 depth of the distributaries.

342 Although these modifications mostly change the DTM of the distributaries in the forested floodplain
343 area (refer to section 3.3 about the names of each area chosen in this study) and not in the Wax Lake
344 delta and main channel, the dynamics of the whole region is affected by those changes. However,
345 the way each station is influenced is different.

346 The results in the stations located in the main channel and delta are mostly dependent on the
347 discharge capacity of the floodplain rather than solely on width and depth of the distributary
348 channels. We found that changing either width or depth of the distributary channels while keeping
349 their cross-sectional area almost constant has the same effect on the hydrodynamic of the Wax Lake
350 outlet, meaning that one of the dominant parameters in the floodplain affecting the main channel is
351 the wetted cross-sectional area of the distributary channels. For example, in Figure 5a, the sensitivity
352 of the station WL5 (as a representative of the stations located along the Wax Lake outlet) to the
353 modification of the bathymetry is presented. During high tide, the sensitivity of the results to DTM
354 modification is small, and all the cases underestimate the water level resulting from tidal flooding.
355 This vertical shift of the model signals compared to the measured ones is related to low roughness
356 coefficient used in WLO (which is corrected in Section 4.2). Focusing on the low-tide periods (because
357 the model is most sensitive to the low-tide water level), it is observed that the results corresponding
358 to narrow 1.5 m deeper and wide 1 m deeper (solid-red and dashed-green signals in Figure 5a) are

359 very close (Figure 5a). Moreover, the overall pattern is that the higher the discharge capacity of the
360 distributary channels, the higher the tidal damping (i.e., lower high water-level and higher low water-
361 level). This may be due to the balance between frictional damping and topographic convergence (Jay,
362 1991). Increasing the discharge capacity of the distributary channels enhances the overall friction in
363 the domain (because more water flows into the shallow distributaries). On the other hand, decrease
364 of the discharge capacity leads to lower overall friction because water is driven to flow mainly in the
365 deeper channels (increase of the system convergence in terms of overall wetted geometry), causing
366 the amplitude of water-level signal to increase. This is why narrow 1 m deeper channels have the
367 highest amplitude while the wide 2.5 m deeper channels have the lowest one. The balance between
368 friction and convergence is a key factor in the tidal properties in each WL station; however, it is not
369 straightforward for the CRMS stations probably due to the effects of other factors such as
370 distributary connectivity.

371 The sensitivity of the CRMS stations to the DTM change is different from one station to the other
372 (Figure 5 and Appendix). Figure 5b-d show three of these behaviors : best results over the CRMS0464
373 station were obtained for narrow channel dug 1.5 m (dashed-green signal in Figure 5b), but the
374 sensitivity of the results become negligible with deeper and/or wider distributaries. This behavior
375 may be due to the effects of the discharge capacity of its nearby lake (i.e., *Belle Isle Lake*). On the
376 other hand, the water level at CRMS4016 is mostly dependent on the depth rather than width (in
377 Figure 8c, compare the solid and dashed lines of the same color, especially the ones in red). The
378 reason is probably due to the fact that it is located along the bank of one of the main distributaries
379 on the eastern side of WLO (between *Myrtle Bayou* and *Coalboat Pass*) and changing the width of
380 the distributaries does not change its connection to the water flow in the region.

381 Station CRMS4808, located in the forested area on the western side of the Wax Lake outlet, has a
382 smaller discharge capacity resulting in larger tidal dampening (with more significant changes at the
383 low tides). It is not straightforward to choose the best case to simulate the ebb-tide periods in this

384 station probably due to the high uncertainty of the bathymetry (especially the distributary bed
385 profile) in its surrounding region. For the high-tide water levels lower than about 0.5 m (not shown in
386 the main text, see Appendix), the model well follows the measurement. Interestingly, at two of the
387 highest high-tide periods during which water level becomes higher than about 0.5 m, all the cases
388 except the narrow-1m deeper case (dashed-red signal in Figure 8d) fail to predict the water-level
389 dampening observed in reality. This may indicate that different mechanisms become dominant in
390 high-energy periods. This behavior only occurs in the presence of vegetation. This area is covered
391 mostly by herbaceous plants such as *Colocasia esculenta* (especially surrounding CRMS4809) and
392 *Nelumbo lutea* (Daniel Jensen, JPL NASA, personal communication, 2018). These plants have a
393 narrow stem with large leaves starting from about 1.5 m above the ground (Okonkwo, 1993) which
394 may increase in their corresponding drag coefficient when water reaches a specific height. For the
395 purpose of this study, we choose to ignore these effects of vegetation because they happen only in
396 two high-tide periods of two of the stations.

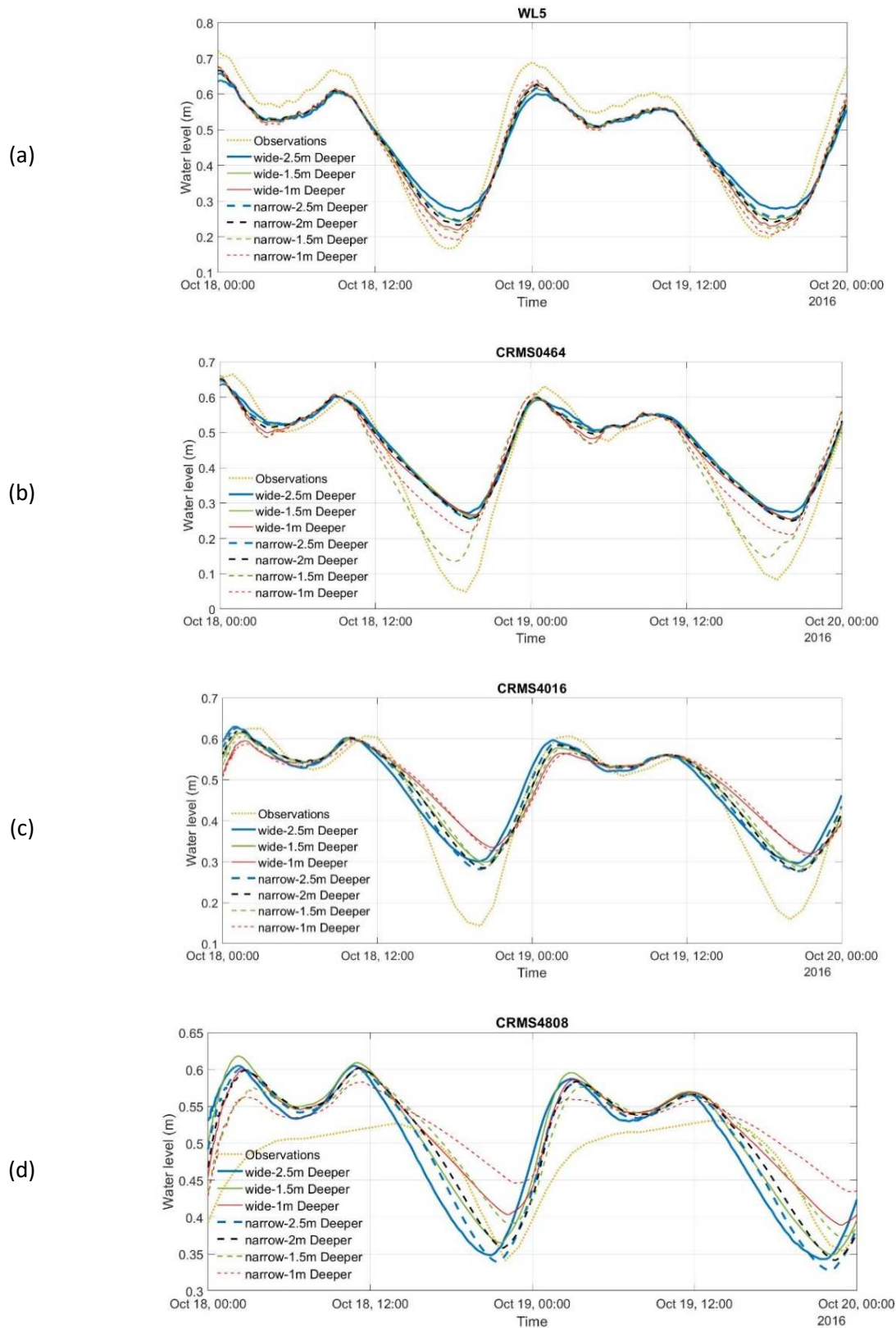
397 In addition, the changes in the DTM causes a slight phase shift in the water-level signal in some of
398 the CRMS stations. This may be due to the decrease of tidal wave celerity which is a function of water
399 depth and friction (Cai et al., 2012). As a complementary to Figure 5, Figure 6 statistically compares
400 the efficiency of each modified DTM in WL1-WL9 and CRMS stations.

401 Considering the analyses explained in this section and the RMSE and R^2 values, the narrow 1.5-meter-
402 depth-correction DTM (explained in section 3.2.1) is chosen to have the best overall results for all of
403 the measurement stations. This DTM will be used in the next stage to further improvement of the
404 model including using spatially-variable bottom-roughness Manning's coefficient and (see Section
405 4.2).

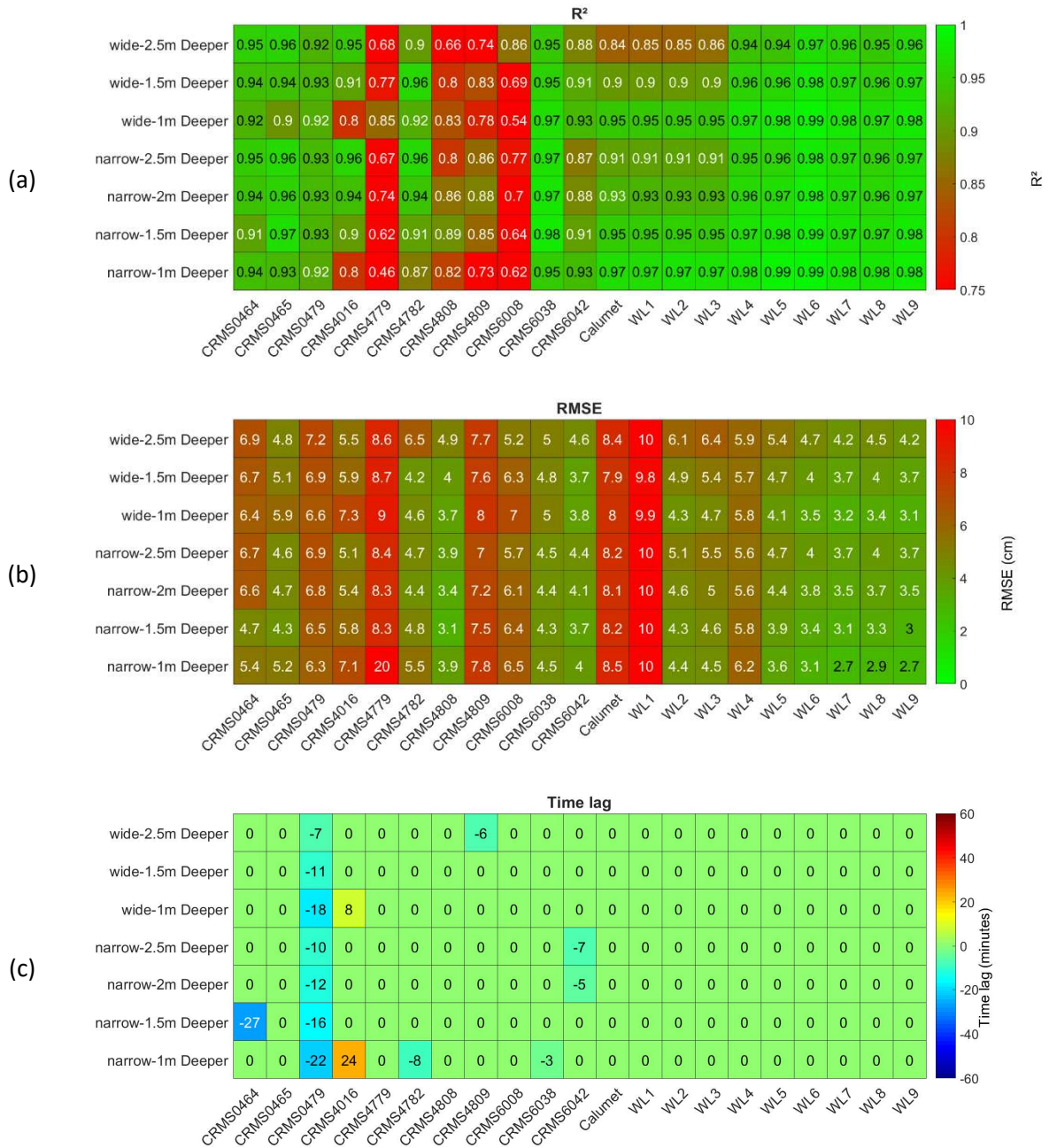
406 Using the narrow 1.5-meter-depth-correction DTM, Figure 7 shows the water-level map at three
407 different instances of the tide, i.e., low tide in the WLO (left), high tide in the WLO (center), and high
408 tide in the floodplain (right). The time-series plot shown at the bottom of this figure corresponds to

409 the water elevation at the ocean boundary. This figure illustrates the delay between the highest
410 water level in the main channels and the one in the floodplain.

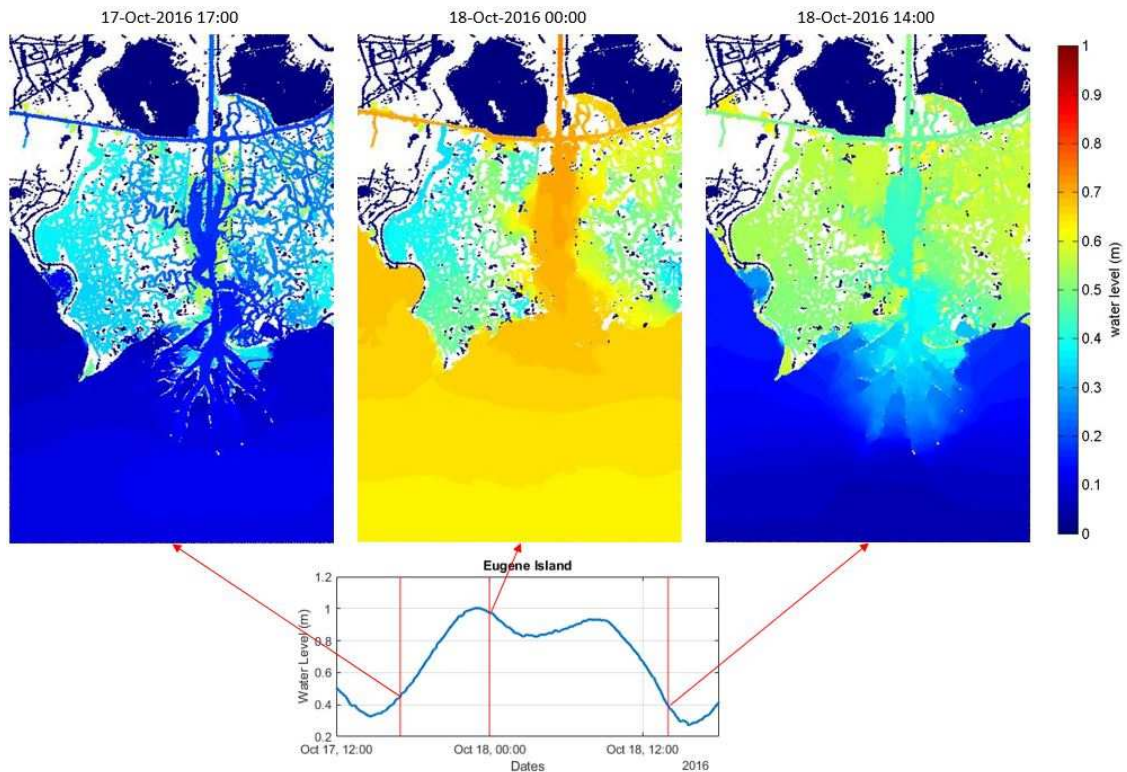
411 As mentioned earlier, it is assumed that overestimation of the low-tide water level (especially in the
412 forested region) is due to the excessive flow resistance due to the uneven bed level along the
413 distributaries. Following an iterative approach and upon using spatially variable Manning's coefficient
414 (explained in the next section), this assumption is tested by manually changing the depth of all the
415 computational cells which are between 1 to 2 meters deep to 1.5 m deep. The resultant decrease in
416 low water level is significant; for example, the drop at one of the low-tides is 7 cm and 4 cm for
417 CRMS4808 and CRMS6008 respectively. In general, however, the results become better for some of
418 the stations such as CRMS6008, but worse for some others (e.g., CRMS4808 especially because of
419 increase in phase lag). This observation confirms that the bed of the distributaries may be flatter in
420 reality than in the DTM and this difference leads to an overestimation of water level at a few stations
421 during low tide. Moreover, it also indicates the increasing the resolution of the grid may not
422 necessarily improve the results since larger grids intrinsically decreases the bed elevation change
423 along the distributaries.



424 *Figure 5 - Comparison and evaluation of the modelled water level time-series in four representative stations (with different*
 425 *behaviors) obtained using the modified DTMs.*



426 Figure 6 comparison of averaged R^2 , RMSE and phase lag values for choosing the best version of DTM modification



427

428 *Figure 7- Simulated flood map of the whole numerical domain at three instants. Left-hand-side map: at low tide in the Wax*
 429 *Lake Outlet. Middle map: at high tide in the Wax lake Outlet. Right-hand-side map: high tide in the floodplain*

430 4.2. Further improvement of the model

431 In this section, the best model chosen from the previous section (i.e., narrow 1.5 m depth correction
 432 DTM) is used to test the effects of spatially-variable bottom roughness and vegetation in the model.
 433 Consequently, the effect of the WLO bottom roughness is examined and the vertical shift of water-
 434 level signal in some of the WL stations is corrected. Additionally, our tests confirm that ignoring the
 435 vegetation effects has been a reasonable assumption in this specific investigation.

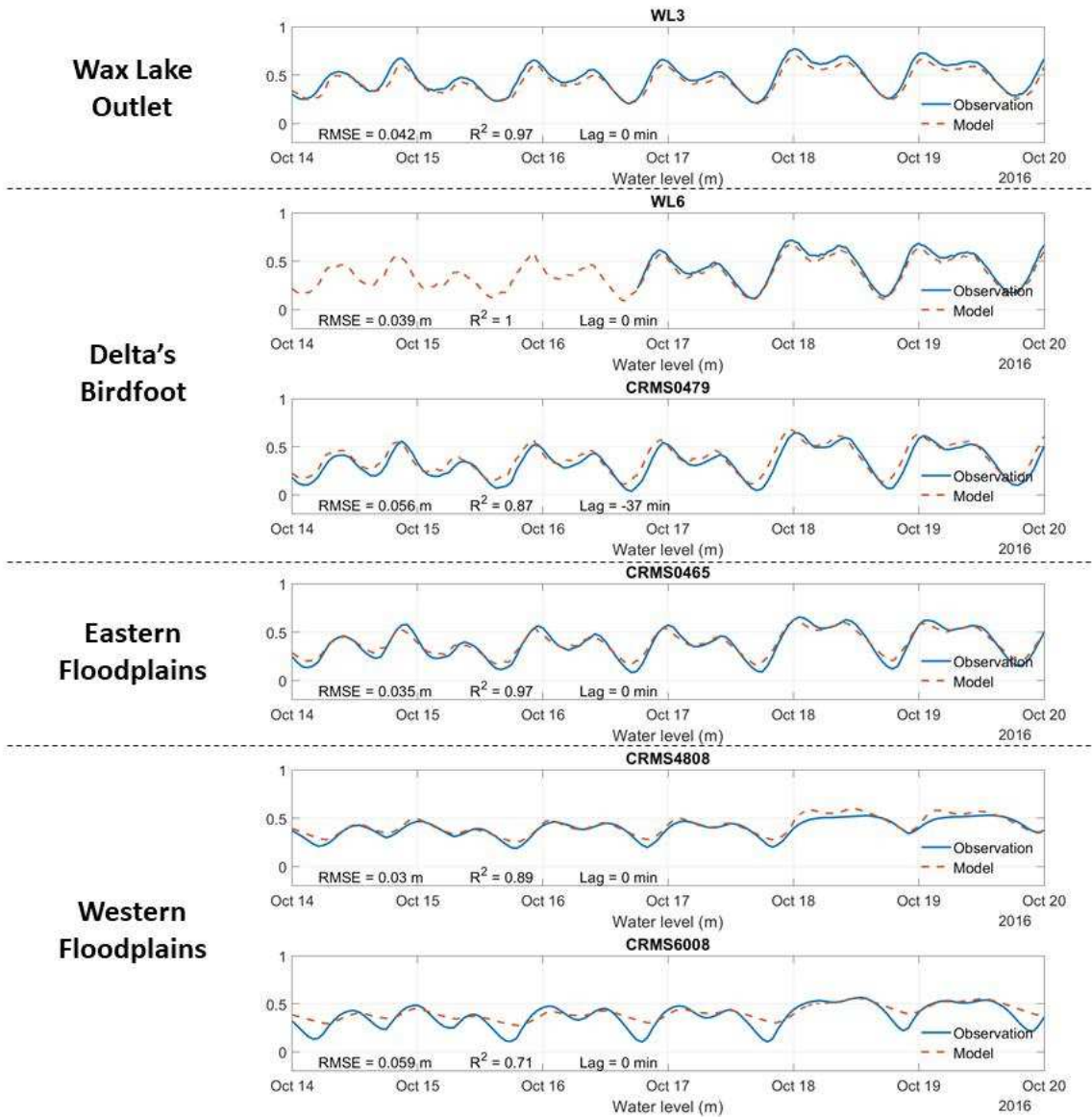
436 For Wax Lake Outlet, higher Manning's roughness coefficient n is used to compensate the decrease
 437 of bottom roughness due to increase of depth (for example, Chow (1959) suggested the Manning's
 438 coefficient of $n=0.03 \text{ s/m}^{1/3}$ for clean, straight, full stage, no rifts or deep pools). Two values of
 439 Manning's coefficient are considered for the WLO: one for the deeper section which is located from
 440 the upstream of WLO down to its cross-section with ICWW, and another for the rest of the river to
 441 WLD (Figure 1c). As a result of this, the upstream water-level signal is shifted upward, especially in
 442 WL1, Calumet and CRMS4782 stations (this shift is also observed in WL3, CRMS6042, and CRMS6038,

443 but the further southward stations are less affected); For the results not shown in Figure 8, see
 444 Appendix. Consistently, the changes of the results in the delta are not remarkable. On the other
 445 hand, higher Manning's roughness coefficient (n) in WLO increases both the high- and low-tide water
 446 levels in the floodplain (with lower sensitivity in the high tide periods); therefore, n must be
 447 increased carefully. Furthermore, for the Wax Lake floodplain, low values of Manning's coefficient
 448 are used to decrease the water level during the low tides. Finally, the Manning's coefficient values
 449 provided in Table 1 are chosen to obtain the results shown in Figure 8 and Appendix.

450 In Figure 8, the respective values of average RMSE, R^2 and lag are also provided for each station. In
 451 comparison to Figure 5, in general, the high tides in the WL stations and the low tides in both sets of
 452 observation points are slightly improved. Figure 8 shows the result of WL3 as a representative station
 453 of the ones along the Wax Lake Outlet. In the delta, Manning's coefficient is $n=0.018 \text{ s/m}^{1/3}$ in the
 454 main fan-shaped channels, and near the river bank, they are either 0.016, 0.014 or 0.012 (depending
 455 on their respective depth). The respective modelled water-level matches well with the measurement.
 456 Interestingly, comparing the results of WL6 and CRMS0479 (which are very close to each other and
 457 their main difference is that CRMS0479 is not in the main Wax Lake Delta channels but a small
 458 distributary) shows that a small distributary can have a remarkable effect on the results (i.e., here
 459 creates a phase lag and prevents the station to be drained enough).

460 *Table 1 Manning's coefficients selected according to depth of the computational cells*

Depth threshold	$22 < d$	$22 < d < 10$	$3 < d < 10$	$2 < d < 3$	$1 < d < 2$	$0 < d < 1$	$d < 0$
Manning's coefficient [$\text{s/m}^{1/3}$]	0.06	0.035	0.018	0.016	0.014	0.012	0.02



461
 462 Figure 8- Evaluation of the calibrated modelled water level time-series in some of the selected
 463 measurement stations

464 Furthermore, as stated in Section 3.4, to examine the effects of vegetation, Baptist 2 formulation is
 465 used in this 2-D model. It resulted in damping the tidal energy, i.e., decreasing the high tide and
 466 increasing the low tide (Rodríguez et al., 2017) throughout the simulation which increases the error
 467 of the model. This trend is compatible with the long inundation time (known as “hydroperiod”)
 468 observed at the two highest crests of the measured water-level signal in the observation stations
 469 CRMS4808 and CRMS4809 (during which the water level exceeds roughly 0.5 m, see Appendix).

470 During these two periods, water becomes almost stagnant with a residence time of roughly 14 hours,
471 which is suggested it may be due to the effects of vegetation.

472 5. Conclusions

473 WLO is a man-made channel with a large floodplain area containing a complex network of
474 distributary channels. This region is relatively flat with a complex intertidal area, making it a suitable
475 study zone to test the remote-sensing and hydrodynamic models in detecting/predicting the tide-
476 induced surface water level change. This study simulates the flood-map evolution of WLO, delta and
477 floodplain during the time period of October 14th, 2016 at 00:00:00 UTC to October 20th, 2016 at
478 00:00:00 UTC under three forcing of tide, river discharge and wind. Modeling results were evaluated
479 by two sets of measurement stations to cover both river and floodplain tidal hydrodynamics.

480 This paper followed a novel approach to tackle the difficulties encountered due to lack of accurate
481 bathymetric data for modeling a tidal-fluvial flat region. It was necessary to modify the original
482 remotely-sensed DTM in order to better represent the distributary channels and thus obtain
483 satisfying results over the floodplain in calm conditions. This task was accomplished by digging
484 distributary channels in the floodplain, following Google Maps' water mask (Google, n.d.).

485 This study aims to provide the data to be used in calibration/validation phase of the SWOT mission.
486 We have successfully calibrated the bathymetry to obtain a reasonably accurate hourly flood-map
487 evolution of the region during one week. Both the grid spatial resolution (i.e., 46 x 45 m²) and the
488 model accuracy are well in the range required by SWOT (i.e., 100x100 m² and 10 cm respectively).
489 The final bathymetry resulting to these data was selected following a sensitivity analysis of the model
490 to the depth and width of the distributaries. Then, the effects of spatially-variable bottom roughness
491 and vegetation were tested.

492 This investigation provides a useful methodology to calibrate the distributaries in a relatively flat
493 intertidal area with a complex network of distributaries; it could be especially useful for future and

494 more extended studies on this region. The model and calibration approach provides a useful tool to
495 understand how the bathymetry and bottom roughness of the distributary channels and WLO
496 bottom roughness contribute to the hydrodynamic of the region.

497 The effect of the width and depth of the distributaries on WLO is related to the discharge capacity of
498 the floodplain. Increasing the discharge capacity of the distributaries results in lower water-level
499 amplitude in the WLO because it means spreading more water in the secondary (shallow) channels
500 relative to the main (deep) channel, thereby increasing of the overall wetted area and roughness.
501 Accordingly, decreasing the discharge capacity brings the water mass towards the Wax Lake outlet,
502 thereby decreasing the overall roughness and increasing the water-level amplitude. On the other
503 hand, in the distributary network of the WLO flood plain, the improvement of the results with
504 changing the DTM varies in different stations and in high- and low-tide periods. It is suggested that
505 the different behavior mainly depend on the position of each station with respect to the main
506 distributaries and ponds, the network of shallow distributaries, and/or vicinity to forested area. The
507 results suggest that the stations located by the main distributaries mainly depend on the depth
508 rather than width and connectivity. However, the stations within the network of shallow
509 distributaries mainly depend on the discharge capacity of the channel cross-section of the
510 distributaries.

511 In general, the calibrated model follows the observed-water-level changes well in the WLO while the
512 main discrepancies occur in the floodplain. Additional tests suggest that flattening the bottom profile
513 along the distributaries improves the results in the floodplain during the low-tide periods. Moreover,
514 adding the effects of vegetation dampens the tidal amplitude which is an increase of the error in
515 majority of the stations (the measurement shows this dampening effect only in two of the stations
516 during two of their highest high tides), suggesting that ignoring the effects of vegetation in this
517 investigation is reasonable, but it may not be the case for more energetic periods.

518 Acknowledgements

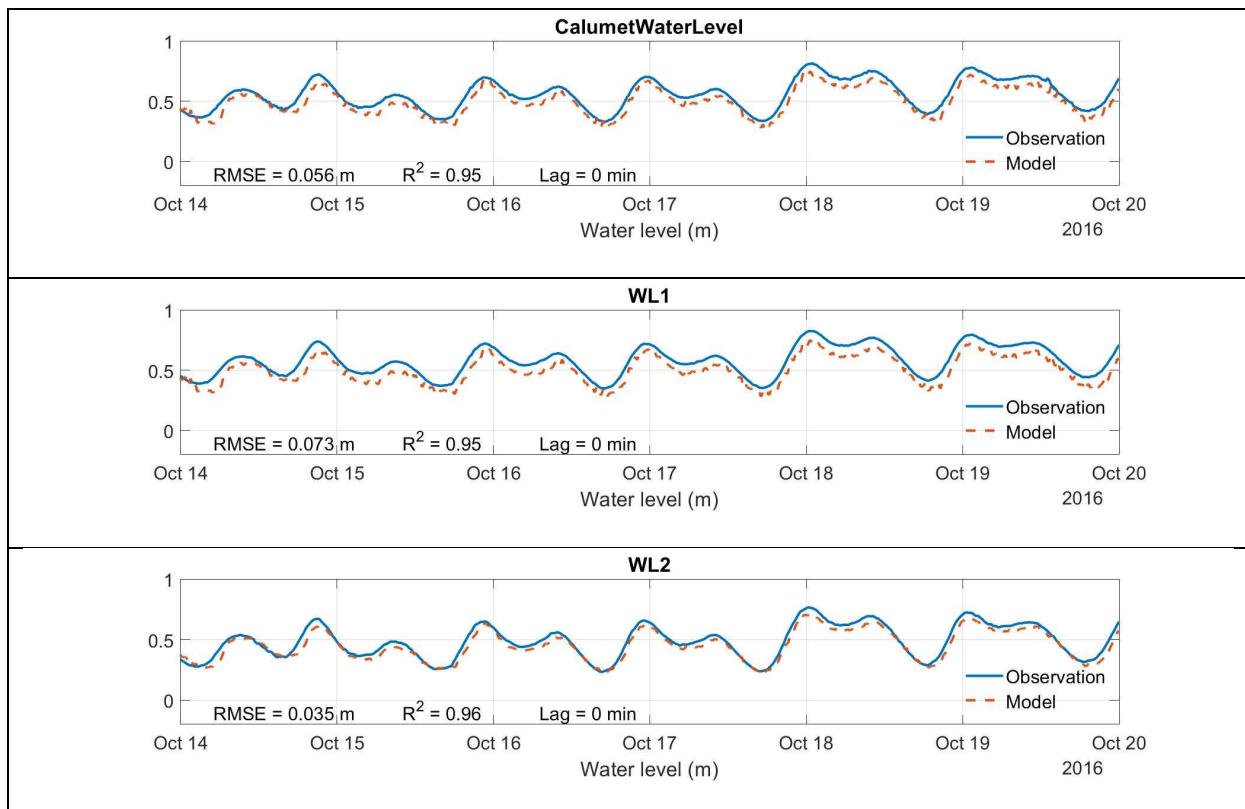
519 The authors are grateful to the COTEST international project funded by CNES-TOSCA, related to the
520 future space mission called Surface Water and Ocean Topography (SWOT).

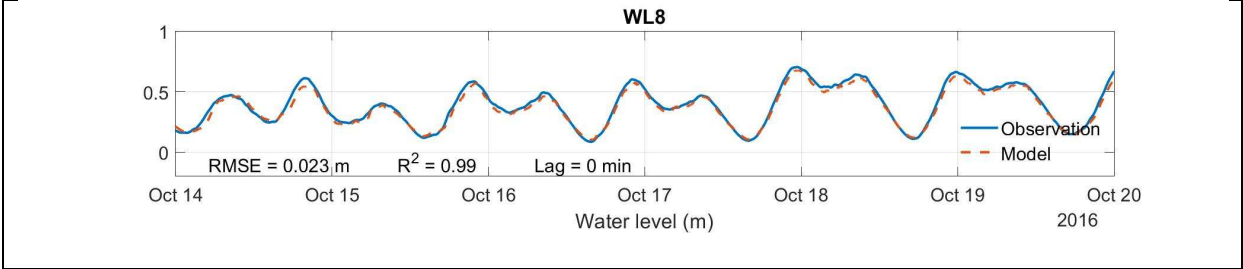
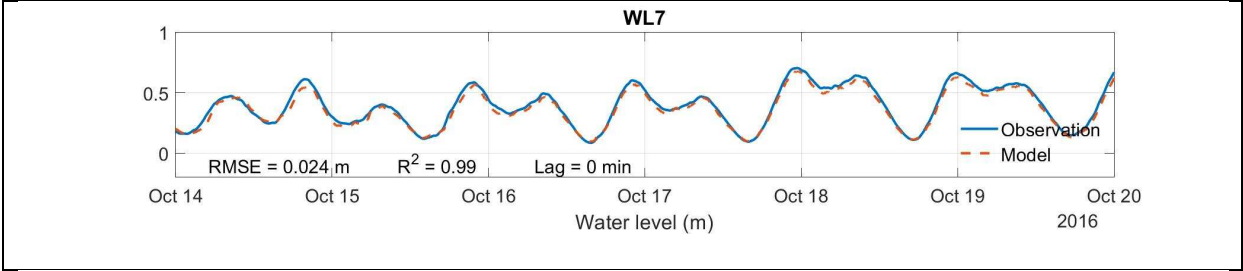
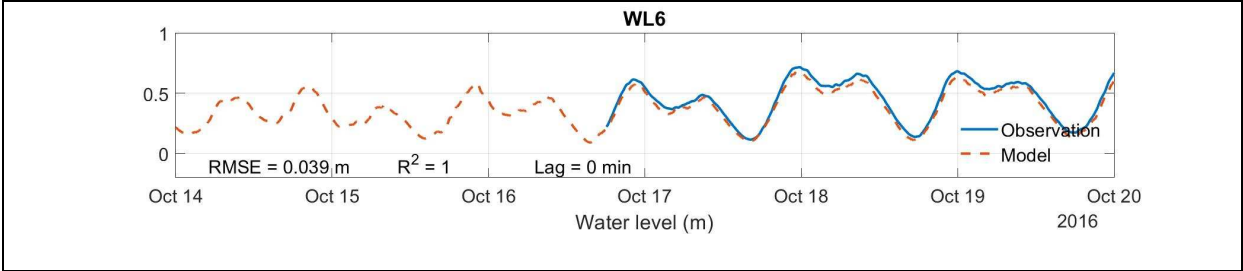
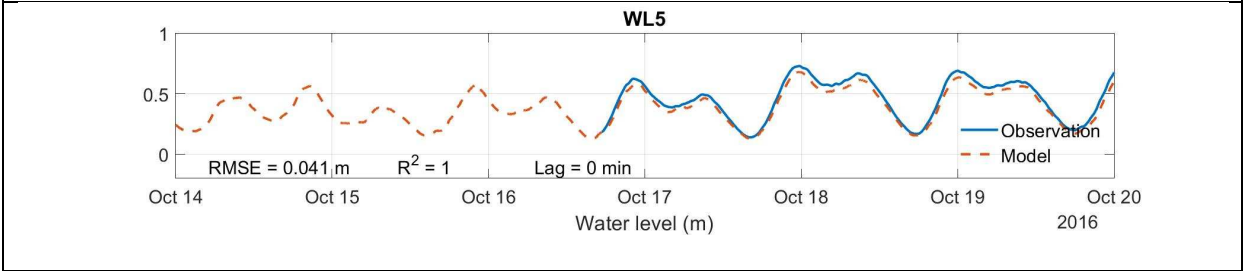
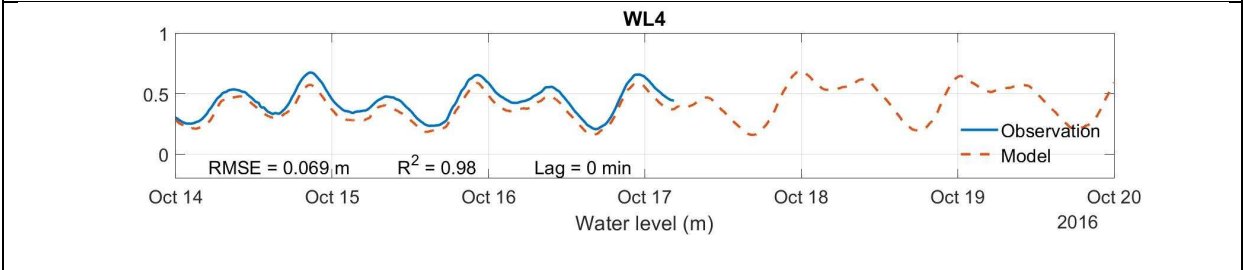
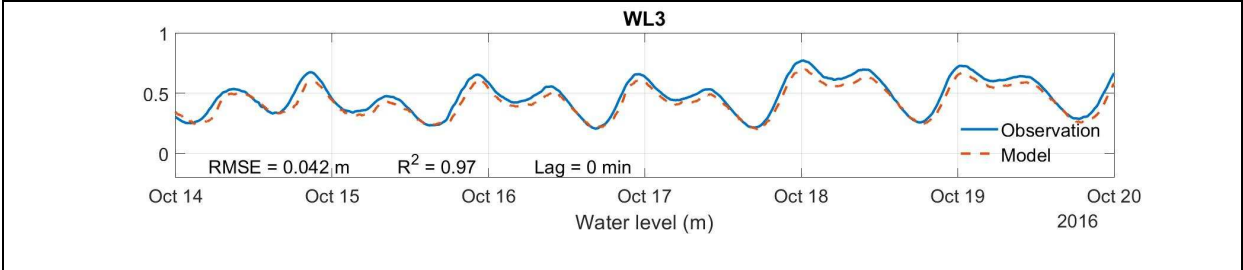
521 This work was partly performed by the Jet Propulsion Laboratory, California Institute of Technology,
522 under contract with the National Aeronautics and Space Administration (NASA). Simard was funded
523 within the framework of the SWOT Science Team, funded by NASA's Physical Oceanography
524 Program.

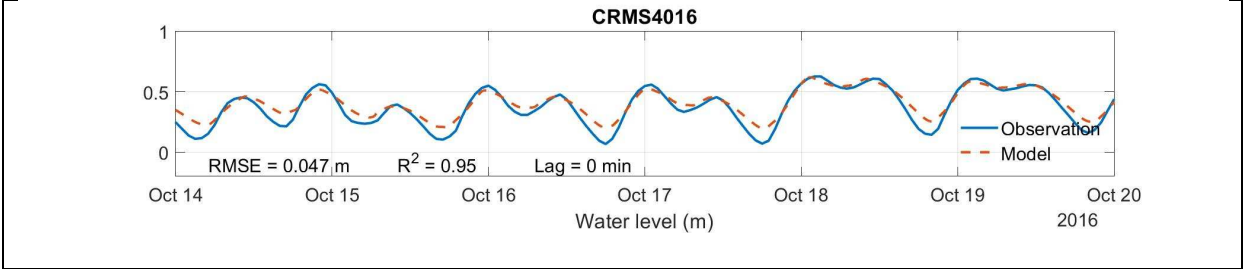
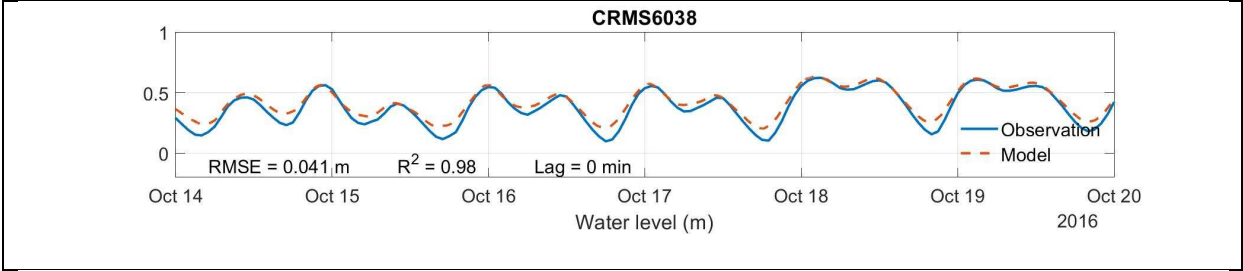
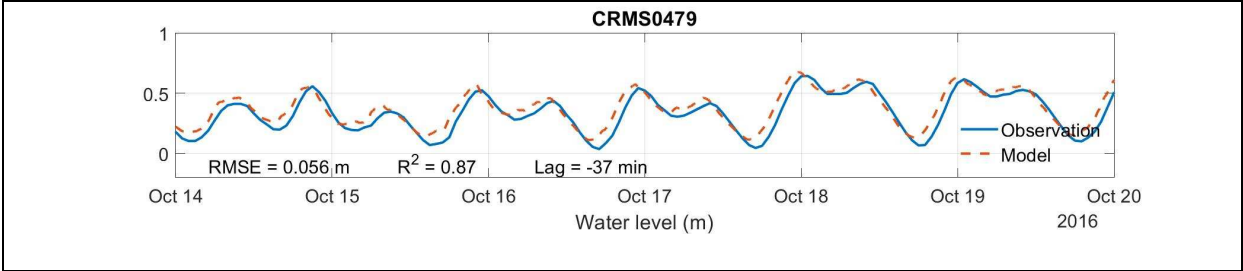
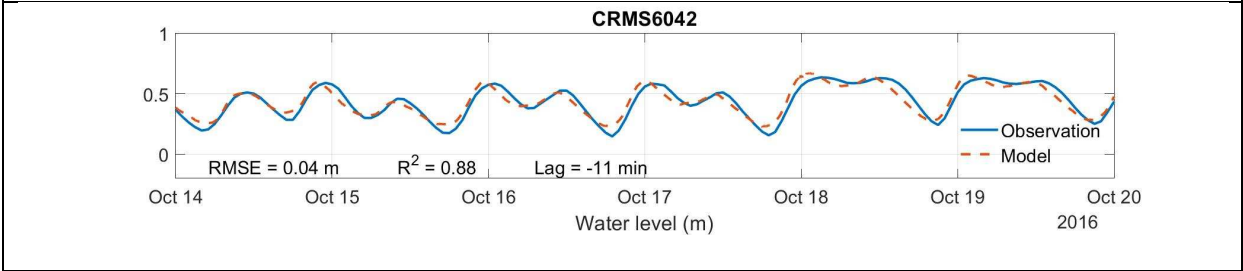
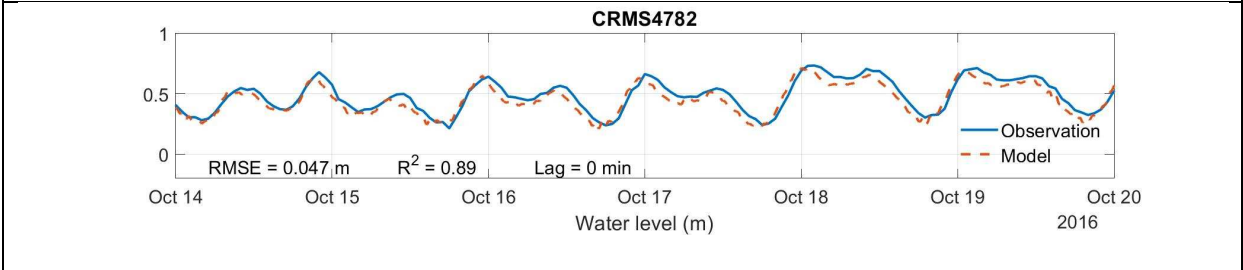
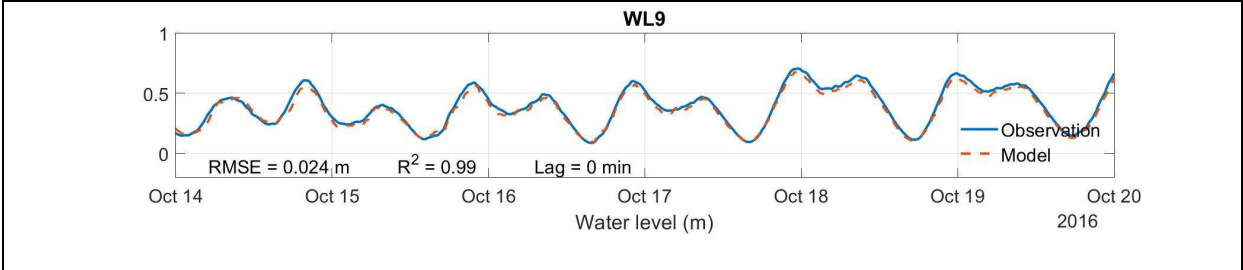
525 The authors also acknowledge USGS, NOAA, and Google for providing the data used for this study
526 including elevation, discharge, water level, and water mask data respectively.

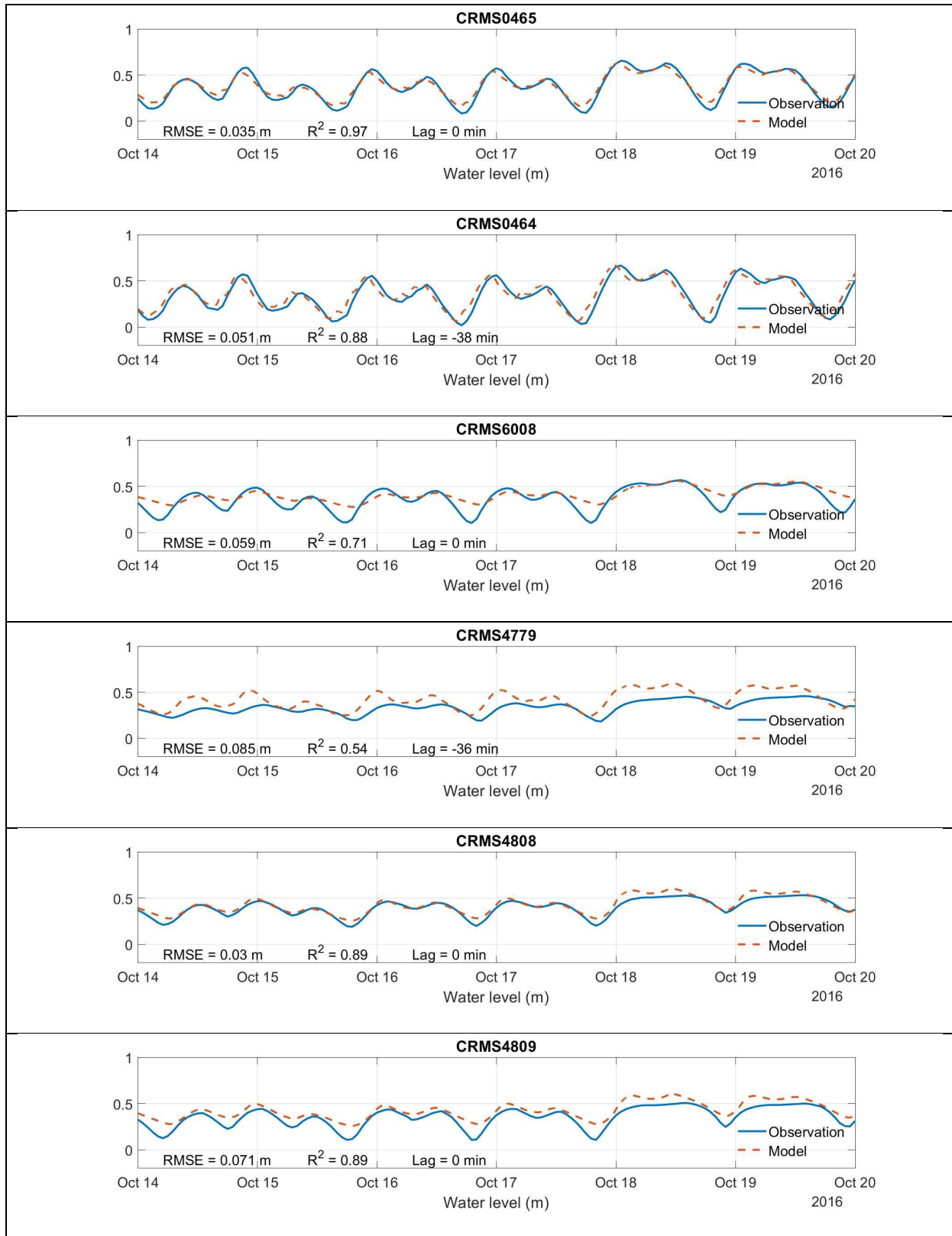
527 Appendix

528 Comparison of the modelled and measured water-level signals obtained by the calibrated DTM
529 including all the studied stations (An extended version of Figure 8).









530

531 [References](#)

532 Al-Asadi, K., & Duan, J. G. (2017). Assessing methods for estimating roughness coefficient in a

533 vegetated marsh area using Delft3D. *Journal of Hydroinformatics*, 19(5), 766–783.

534 Baptist, M. J., Babovic, V., Rodríguez Uthurburu, J., Keijzer, M., Uittenbogaard, R. E., Mynett, A., &
535 Verwey, A. (2007). On inducing equations for vegetation resistance. *Journal of Hydraulic*
536 *Research*, 45(4), 435–450.

537 Barbier, E. B., Georgiou, I. Y., Enchelmeyer, B., & Reed, D. J. (2013). The Value of Wetlands in
538 Protecting Southeast Louisiana from Hurricane Storm Surges. *PLoS ONE*, 8(3), e58715.
539 <https://doi.org/10.1371/journal.pone.0058715>

540 Buschman, F. A., Hoitink, A. J. F., Van Der Vegt, M., & Hoekstra, P. (2010). Subtidal flow division at a
541 shallow tidal junction. *Water Resources Research*, 46(12).

542 Cai, H., Savenije, H. H. G., Yang, Q., Ou, S., & Lei, Y. (2012). Influence of river discharge and dredging
543 on tidal wave propagation: Modaomen Estuary case. *Journal of Hydraulic Engineering*, 138(10),
544 885–896.

545 Carle, M. M. (2013). *Spatial Structure and Dynamics of the Plant Communities in a Pro-grading River*
546 *Delta: Wax Lake Delta, Atchafalaya Bay, Louisiana. December.*

547 Chow, V. Te. (1959). *Open-channel hydraulics*. McGraw-Hill.

548 Christensen, A. (2017). Hydrodynamic Modeling of Newly Emergent Coastal Deltaic Floodplains. In
549 *Louisiana State University Master Thesis* (Issue December).

550 Davidson, R. A., States., U., & Station., U. S. A. E. W. E. (1988). *Wax Lake Outlet control structure,*
551 *Louisiana: hydraulic model investigation* (pp. 15, [31] pages). Waterways Experiment Station.

552 Deltares, D. (2014). *Delft3D-FLOW user manual*. Deltares.

553 Denbina, M., Simard, M., Rodriguez, E., Wu, X., Chen, A., & Pavelsky, T. (2019). Mapping water
554 surface elevation and slope in the Mississippi River Delta using the AirSWOT Ka-band
555 interferometric synthetic aperture radar. *Remote Sensing*, 11(23), 1–26.

556 <https://doi.org/10.3390/rs11232739>

557 Denbina, M. W., Simard, M., Pavelsky, T. M., Christensen, A. I., Liu, K., & Lyon, C. (2020). *Pre-Delta-X:*
558 *Channel Bathymetry of the Atchafalaya Basin, LA, USA, 2016*. ORNL Distributed Active Archive
559 Center. <https://doi.org/10.3334/ORNLDAAAC/1807>

560 Durand, M., Fu, L.-L., Lettenmaier, D. P., Alsdorf, D. E., Rodriguez, E., & Esteban-Fernandez, D. (2010).
561 The surface water and ocean topography mission: Observing terrestrial surface water and
562 oceanic submesoscale eddies. *Proceedings of the IEEE*, 98(5), 766–779.

563 Edmonds, D. A., & Slingerland, R. L. (2007). Mechanics of river mouth bar formation: Implications for
564 the morphodynamics of delta distributary networks. *Journal of Geophysical Research: Earth*
565 *Surface*, 112(F2).

566 Gaultier, L., Ubelmann, C., & Fu, L.-L. (2010). SWOT simulator documentation. *Rapp. Tech. JPL, NASA*.

567 Gerritsen, H., Goede, E. D. d., Platzek, F. W., Kester, J. A. T. M. van, Genseberger, M., &
568 Uittenbogaard, R. E. (2008). *Validation Document Delft3D- FLOW Validation Document Delft3D-*
569 *FLOW*. Deltares.

570 Gesch, D. B., Evans, G. A., Oimoen, M. J., & Arundel, S. T. (2002). The National Elevation Dataset. In
571 *Digital Elevation Model Technologies and Applications: The DEM Users Manual* (Issue 68, pp. 5–
572 32).

573 Gomez-Navarro, L., Fablet, R., Mason, E., Pascual, A., Mourre, B., Cosme, E., & Le Sommer, J. (2018).
574 SWOT spatial scales in the western Mediterranean sea derived from pseudo-observations and
575 an Ad Hoc filtering. *Remote Sensing*, 10(4), 599.

576 Google. (n.d.). *Google Maps*.

577 Gross, T. F., & Werner, F. E. (1994). Residual circulations due to bottom roughness variability under
578 tidal flows. *Journal of Physical Oceanography*, 24(7), 1494–1502.

579 Hanegan, K. C. (2011). *Modeling the Evolution of the Wax Lake Delta in Atchafalaya Bay, Louisiana*.

580 Hiatt, M. R. (2013). *A network-based analysis of river delta surface hydrology: an example from Wax*
581 *Lake Delta*.

582 Hoitink, A. J. F., & Jay, D. A. (2016). Tidal river dynamics: Implications for deltas. *Reviews of*
583 *Geophysics*, 54(1), 240–272.

584 Horstman, E. M., Bryan, K. R., Mullarney, J. C., Pilditch, C. A., & Eager, C. A. (2018). Are flow-
585 vegetation interactions well represented by mimics? A case study of mangrove
586 pneumatophores. *Advances in Water Resources*, 111, 360–371.

587 Horstman, E. M., Dohmen-Janssen, C. M., Narra, P. M. F., Van den Berg, N. J. F., Siemerink, M., &
588 Hulscher, S. J. M. H. (2014). Wave attenuation in mangroves: A quantitative approach to field
589 observations. *Coastal Engineering*, 94, 47–62.

590 Hu, K., Chen, Q., & Wang, H. (2015). A numerical study of vegetation impact on reducing storm surge
591 by wetlands in a semi-enclosed estuary. *Coastal Engineering*, 95, 66–76.

592 Jay, D. A. (1991). Green's law revisited: Tidal long-wave propagation in channels with strong
593 topography. *Journal of Geophysical Research: Oceans*, 96(C11), 20585–20598.

594 Jay, D. A., Borde, A. B., & Diefenderfer, H. L. (2016). Tidal-fluvial and estuarine processes in the Lower
595 Columbia River: II. Water level models, floodplain wetland inundation, and system zones.
596 *Estuaries and Coasts*, 39(5), 1299–1324.

597 Jay, D. A., Leffler, K., Diefenderfer, H. L., & Borde, A. B. (2015). Tidal-fluvial and estuarine processes in
598 the lower Columbia River: I. Along-channel water level variations, Pacific Ocean to Bonneville
599 Dam. *Estuaries and Coasts*, 38(2), 415–433.

600 Jung, H. C., & Jasinski, M. F. (2015). Sensitivity of a floodplain hydrodynamic model to satellite-based
601 DEM scale and accuracy: Case study—The Atchafalaya Basin. *Remote Sensing*, 7(6), 7938–7958.

602 Kathiresan, K., & Rajendran, N. (2005). Coastal mangrove forests mitigated tsunami. *Estuarine,*
603 *Coastal and Shelf Science, 65*(3), 601–606.

604 Kim, W., Mohrig, D., Twilley, R., Paola, C., & Parker, G. (2009). Is it feasible to build new land in the
605 Mississippi River Delta? *Eos, Transactions American Geophysical Union, 90*(42), 373–374.

606 Leonardi, N., Kolker, A. S., & Fagherazzi, S. (2015). Interplay between river discharge and tides in a
607 delta distributary. *Advances in Water Resources, 80*, 69–78.

608 Lesser, G. R., Roelvink, J. A. v, Van Kester, J., & Stelling, G. S. (2004). Development and validation of a
609 three-dimensional morphological model. *Coastal Engineering, 51*(8–9), 883–915.

610 Makaske, B., Maas, G. J., Van den Brink, C., & Wolfert, H. P. (2011). The influence of floodplain
611 vegetation succession on hydraulic roughness: is ecosystem rehabilitation in Dutch embanked
612 floodplains compatible with flood safety standards? *Ambio, 40*(4), 370–376.

613 Marsooli, R., Orton, P. M., Georgas, N., & Blumberg, A. F. (2016). Three-dimensional hydrodynamic
614 modeling of coastal flood mitigation by wetlands. *Coastal Engineering, 111*, 83–94.

615 Mcleod, E., Chmura, G. L., Bouillon, S., Salm, R., Björk, M., Duarte, C. M., Lovelock, C. E., Schlesinger,
616 W. H., & Silliman, B. R. (2011). A blueprint for blue carbon: toward an improved understanding
617 of the role of vegetated coastal habitats in sequestering CO₂. *Frontiers in Ecology and the*
618 *Environment, 9*(10), 552–560.

619 Megonigal, J. P., & Neubauer, S. C. (2019). Biogeochemistry of tidal freshwater wetlands. In *Coastal*
620 *Wetlands* (pp. 641–683). Elsevier.

621 Nardin, W., Edmonds, D. A., & Fagherazzi, S. (2016). Influence of vegetation on spatial patterns of
622 sediment deposition in deltaic islands during flood. *Advances in Water Resources, 93*, 236–248.

623 Neeck, S. P., Lindstrom, E. J., Vaze, P. V., & Fu, L.-L. (2012). Surface water and ocean topography
624 (SWOT) mission. *Sensors, Systems, and Next-Generation Satellites XVI, 8533*, 85330G.

625 Nicholls, R. J., Wong, P. P., Burkett, V., Codignotto, J., Hay, J., McLean, R., Ragoonaden, S., Woodroffe,
626 C. D., Abuodha, P. A. O., & Arblaster, J. (2007). *Coastal systems and low-lying areas*.

627 Okonkwo, C. A. C. (1993). Taro. In *Genetic Improvement of Vegetable Crops* (pp. 709–715).
628 <https://doi.org/10.1016/b978-0-08-040826-2.50052-7>

629 Olliver, E. A., & Edmonds, D. A. (2017). Defining the ecogeomorphic succession of land building for
630 freshwater, intertidal wetlands in Wax Lake Delta, Louisiana. *Estuarine, Coastal and Shelf*
631 *Science*, 196, 45–57. <https://doi.org/10.1016/j.ecss.2017.06.009>

632 Osorio-Cano, J. D., Alcérreca-Huerta, J. C., Mariño-Tapia, I., Osorio, A. F., Acevedo-Ramírez, C.,
633 Enriquez, C., Costa, M., Pereira, P., Mendoza, E., & Escudero, M. (2019). Effects of roughness
634 loss on reef hydrodynamics and coastal protection: approaches in Latin America. *Estuaries and*
635 *Coasts*, 42(7), 1742–1760.

636 Parker, G., & Sequeiros, O. (2006). Large scale river morphodynamics: Application to the Mississippi
637 Delta. *River Flow 2006: Proceedings of the International Conference on Fluvial Hydraulics*, 3–11.

638 Rivera-Monroy, V. H., Twilley, R. R., Davis III, S. E., Childers, D. L., Simard, M., Chambers, R., Jaffe, R.,
639 Boyer, J. N., Rudnick, D. T., & Zhang, K. (2011). The role of the Everglades Mangrove Ecotone
640 Region (EMER) in regulating nutrient cycling and wetland productivity in south Florida. *Critical*
641 *Reviews in Environmental Science and Technology*, 41(S1), 633–669.

642 Rodríguez, J. F., Saco, P. M., Sandi, S., Saintilan, N., & Riccardi, G. (2017). Potential increase in coastal
643 wetland vulnerability to sea-level rise suggested by considering hydrodynamic attenuation
644 effects. *Nature Communications*, 8(1), 1–12.

645 Roelvink, J. A., & Van Banning, G. (1995). Design and development of DELFT3D and application to
646 coastal morphodynamics. *Oceanographic Literature Review*, 11(42), 925.

647 Rouse Jr, L. J., Roberts, H. H., & Cunningham, R. H. W. (1978). Satellite observation of the subaerial
648 growth of the Atchafalaya Delta, Louisiana. *Geology*, 6(7), 405–408.

649 Sassi, M. G., Hoitink, A. J. F., de Brye, B., Vermeulen, B., & Deleersnijder, E. (2011). Tidal impact on
650 the division of river discharge over distributary channels in the Mahakam Delta. *Ocean*
651 *Dynamics*, 61(12), 2211–2228.

652 Shaffer, G. P., & Sasser, C. E. (2018). *Vegetation Dynamics in the Emerging Atchafalaya Delta ,*
653 *Louisiana , USA Author (s): Gary P . Shaffer , Charles E . Sasser , James G . Gosselink and Marcel*
654 *Rejmanek Published by : British Ecological Society Stable URL :*
655 *https://www.jstor.org/stable/22608. 80(4), 677–687.*

656 Shaw, J. B., Mohrig, D., & Wagner, R. W. (2016). Flow patterns and morphology of a prograding river
657 delta. *Journal of Geophysical Research: Earth Surface*, 121(2), 372–391.

658 Shields, M. R., Bianchi, T. S., Mohrig, D., Hutchings, J. A., Kenney, W. F., Kolker, A. S., & Curtis, J. H.
659 (2017). Carbon storage in the Mississippi River delta enhanced by environmental engineering.
660 *Nature Geoscience*, 10(11), 846–851.

661 Sievers, M., Brown, C. J., Tulloch, V. J. D., Pearson, R. M., Haig, J. A., Turschwell, M. P., & Connolly, R.
662 M. (2019). The role of vegetated coastal wetlands for marine megafauna conservation. *Trends*
663 *in Ecology & Evolution*, 34(9), 807–817.

664 Simard, M, Denbina, M. W., Jensen, D. J., & Lane, R. (2020). *Pre-Delta-X: Water Levels across Wax*
665 *Lake Outlet, Atchafalaya Basin, LA, USA, 2016. ORNL DAAC, Oak Ridge, Tennessee, USA.*

666 Simard, Marc, Denbina, M. W., Laignel, B., Liao, T.-H., & Soloy, A. (2019). Remote Sensing of the
667 hydrological processes in the Mississippi River Delta with the SWOT and Delta-X Missions. *AGU*
668 *Fall Meeting Abstracts, 2019, OS23B-1785.*

669 Stelling, G. S., & Van Kester, J. A. T. M. (1994). On the approximation of horizontal gradients in sigma
670 co-ordinates for bathymetry with steep bottom slopes. *International Journal for Numerical*
671 *Methods in Fluids*, 18(10), 915–935.

672 Steyer, G. D. (2010). Coastwide Reference Monitoring System (CRMS). In *Fact Sheet.*

673 <https://doi.org/10.3133/fs20103018>

674 Stone, B. M., & Shen, H. T. (2002). Hydraulic resistance of flow in channels with cylindrical roughness.
675 *Journal of Hydraulic Engineering*, 128(5), 500–506.

676 Temmerman, S., Bouma, T. J., Van de Koppel, J., Van der Wal, D., De Vries, M. B., & Herman, P. M. J.
677 (2007). Vegetation causes channel erosion in a tidal landscape. *Geology*, 35(7), 631–634.

678 Thomas, N., Simard, M., Castañeda-Moya, E., Byrd, K., Windham-Myers, L., Bevington, A., & Twilley,
679 R. R. (2019). High-resolution mapping of biomass and distribution of marsh and forested
680 wetlands in southeastern coastal Louisiana. *International Journal of Applied Earth Observation*
681 *and Geoinformation*, 80, 257–267.

682 Whaling, A., & Shaw, J. (2020). Changes to Subaqueous Delta Bathymetry Following a High River Flow
683 Event, Wax Lake Delta, USA. *Estuaries and Coasts*, 43, 1923–1938.

684 Xie, D., An, S., & Davis, J. A. (2019). Preface: Coastal wetlands: services, uses, and conservation.
685 *Hydrobiologia*, 827(1), 1–2.

686 Xing, F., Kettner, A. J., Syvitski, J. P., Ye, Q., Bevington, A., Twilley, R., & Atkinson, J. H. (2013). Impact
687 of vegetation on the hydrodynamics and morphological changes of the Wax Lake Delta during
688 hurricanes. *AGUFM*, 2013, EP13A-0857.

689 Xing, Fei, Syvitski, J., Kettner, A., Meselhe, E., Atkinson, J., & Khadka, A. (2017). Morphological
690 responses of the Wax Lake Delta, Louisiana, to Hurricanes Rita. *Elem Sci Anth*, 5.

691 Zhang, Q. (2015). *Numerical simulation of cold front-related hydrodynamics of Wax Lake Delta*.

692